

# 1 Development of a High-Resolution Integrated Emission Inventory of 2 Air Pollutants for China

3 Nana Wu<sup>1</sup>, Guannan Geng<sup>2,3\*</sup>, Ruochong Xu<sup>1</sup>, Shigan Liu<sup>1</sup>, Xiaodong Liu<sup>2</sup>, Qinren Shi<sup>2</sup>, Ying Zhou<sup>4</sup>, Yu  
4 Zhao<sup>5</sup>, Huan Liu<sup>2,3</sup>, Yu Song<sup>6</sup>, Junyu Zheng<sup>7</sup>, Qiang Zhang<sup>1</sup>, and Kebin He<sup>2,8</sup>

5 <sup>1</sup>Ministry of Education Key Laboratory for Earth System Modeling, Department of Earth System Science, Tsinghua University,  
6 Beijing 100084, China

7 <sup>2</sup>State Key Joint Laboratory of Environment Simulation and Pollution Control, School of Environment, Tsinghua University,  
8 Beijing 100084, China

9 <sup>3</sup>State Environmental Protection Key Laboratory of Sources and Control of Air Pollution Complex, Beijing 100084, China

10 <sup>4</sup>Key Laboratory of Beijing on Regional Air Pollution Control, Faculty of Environment and Life, Beijing University of  
11 Technology, Beijing, 100124, China

12 <sup>5</sup>State Key Laboratory of Pollution Control and Resource Reuse and School of the Environment, Nanjing University, 163  
13 Xianlin Rd., Nanjing, Jiangsu 210023, China

14 <sup>6</sup>State Key Joint Laboratory of Environmental Simulation and Pollution Control, College of Environmental Sciences and  
15 Engineering, Peking University, Beijing 100871, PR China

16 <sup>7</sup>Sustainable Energy and Environmental Thrust, The Hong Kong University of Science and Technology (Guangzhou),  
17 Guangzhou, 511458, China

18 <sup>8</sup>Institute for Carbon Neutrality, Tsinghua University, Beijing 100084, China

19 *Correspondence to:* Guannan Geng (guannangeng@tsinghua.edu.cn)

20 **Abstract.** Constructing a highly-resolved comprehensive emission dataset for China is challenging due to limited availability  
21 of refined information for parameters in a unified bottom-up framework. Here, by developing an integrated modeling  
22 framework, we harmonized multi-source heterogeneous data including several up-to-date emission inventories at national and  
23 regional scale, and for key species and sources in China, to generate a 0.1 °resolution inventory for 2017. By source mapping,  
24 species mapping, temporal disaggregation, spatial allocation and spatial-temporal coupling, different emission inventories are  
25 normalized in terms of source categories, chemical species, and spatiotemporal resolutions. This achieves the coupling of  
26 multi-scale, high-resolution emission inventories with the MEIC (Multi-resolution Emission Inventory for China), forming a  
27 high-resolution INTegrated emission inventory of Air pollutants for China (i.e., INTAC). We find that the INTAC provides  
28 more accurate representations for emission magnitudes and spatiotemporal patterns. In 2017, China's emissions of SO<sub>2</sub>, NO<sub>x</sub>,  
29 CO, NMVOC, NH<sub>3</sub>, PM<sub>10</sub>, PM<sub>2.5</sub>, BC, and OC are 12.3, 24.5, 141.0, 27.9, 9.2, 11.1, 8.4, 1.3 and 2.2 Tg, respectively. The  
30 proportion of point source emissions for SO<sub>2</sub>, PM<sub>10</sub>, NO<sub>x</sub>, PM<sub>2.5</sub> increases from 7–19% in MEIC to 48–66% in INTAC,  
31 resulting in improved spatial accuracy, especially mitigating overestimations in densely populated areas. Compared to MEIC,  
32 INTAC reduces mean biases in simulated concentrations of major air pollutants by 2–14 µg/m<sup>3</sup> across 74 cities against ground  
33 observations. The enhanced model performance by INTAC was particularly evident at finer grid resolutions. Our new dataset  
34 is accessible at <http://meicmodel.org.cn/intac>, and it will provide a solid data foundation for fine-scale atmospheric research  
35 and air quality improvement.

36

## 37 **1 Introduction**

38 In recent years, China has achieved remarkable progress in improving air quality and public health through the active  
39 implementation of clean air policies (Liu et al., 2020; Xiao et al., 2022; Zhang and Geng, 2019; Zhang et al., 2019a). To further  
40 unlock the potential of targeted clean air actions, there is an urgent need for an accurate and detailed depiction for emissions,  
41 encompassing their magnitudes and spatial-temporal patterns. Developing a reliable highly-resolved emission inventory for  
42 China is also crucial for studies of atmospheric chemistry and climate change (Cheng et al., 2021a; Geng et al., 2021; Zhang  
43 et al., 2019a).

44 The construction of high-resolution emission inventories for China poses significant challenges due to the diversity and  
45 complexity of emission sources and technology distributions. Additionally, the limited availability of localized measurements  
46 for emission factors (EFs) and source profiles, along with exact location of the emission facilities, further compounds the  
47 difficulties (Li et al., 2017a). The widely-used bottom-up approach involves the establishment of a unified framework that  
48 encompasses source categories, chemical speciation processes, spatial-temporal allocation profiles and emission estimation  
49 methods (An et al., 2021; Huang et al., 2021). However, achieving both wide coverage and high accuracy in compiling an  
50 emission inventory for China through this approach remains a formidable task for individual research institutions.

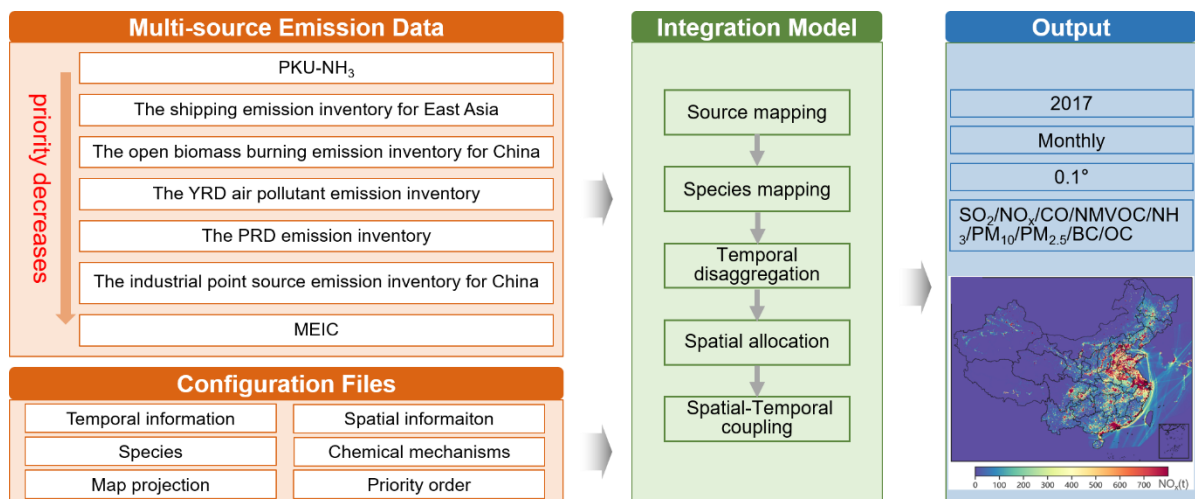
51 Comprehensive national-scale emission inventories developed using the unified framework typically provide extensive  
52 coverage of space, species and sectors (Li et al., 2017a; Li et al., 2023b), but tend to exhibit limitations in spatial accuracy (Wu  
53 et al., 2021; Zhao et al., 2015; Zheng et al., 2021; Zhou et al., 2017b). Previous studies have indicated that the spatial allocation  
54 in large-scale emission inventories rely on spatial proxies (e.g., population, road networks) rather than latitude-longitude  
55 coordinates of emission sources due to the unavailability of extensive spatial information (Li et al., 2017b; Zhang et al., 2009).  
56 The assumption of a linear correlation between emissions and spatial proxies might lead to an overestimation of emissions in  
57 urban areas, especially at scales finer than  $0.25^\circ$  (Wu et al., 2021; Zheng et al., 2021; Zheng et al., 2017). Biases introduced  
58 by the proxy-based method are found to be propagated as the grid size diminishes, resulting in uncertainties for chemical  
59 transport models (CTMs) (Zheng et al., 2021; Zheng et al., 2017).

60 Emission inventories focused on a specific region (An et al., 2021; Huang et al., 2021; Liu et al., 2018), sector (Chen et al.,  
61 2016; Deng et al., 2020; Zhou et al., 2017a) or key species (Huang et al., 2012b; Li et al., 2021; Wang et al., 2023) under the  
62 aforementioned unified framework demonstrate enhanced accuracy, but fail to achieve comprehensive coverage. These  
63 inventories assimilate substantial detailed foundational data from various statistical dataset, on-site measurements or surveys  
64 to represent real-world emission magnitudes, including energy consumption, removal efficiencies, and localized speciation  
65 profile (An et al., 2021; Huang et al., 2021; Liu et al., 2018). Innovative data, such as measurements from continuous emission  
66 monitoring systems (Bo et al., 2021; Tang et al., 2023; Wu et al., 2022), or methodologies like process-based models (Kang  
67 et al., 2016; Zhao et al., 2020) are implemented to enable a more accurate characterization of complex emission dynamics.  
68 Facility-level geographic location is incorporated to optimize the representation of spatial patterns (Liu et al., 2015a; Wang et

69 al., 2019; Wu et al., 2023). The reliability of these local-scale, sector- or species-specified inventories has been validated  
70 against satellite and ground-based measurements (Liu et al., 2016a; Zhang et al., 2021; Zheng et al., 2019).  
71 The other strategy for developing bottom-up emission inventories is commonly known as the integrated method. This method  
72 consolidates multiple emission datasets for specific regions, species or sectors into a unified product, ensuring extensive  
73 coverage (Li et al., 2017b). Taking advantage of existing inventories derived from localized data and advanced methods, the  
74 integrated method facilitates the efficient generation of highly-resolved emission inventories at large scales. However, the  
75 heterogeneity of different emission datasets presents challenges for the fusion, manifested in diverse data formats, sector  
76 categories, species, spatial-temporal resolution. In recent years, there has been growing interest in adopting the integrated  
77 approach to enrich inventories with local insights, particularly at the global (Crippa et al., 2023; Janssens-Maenhout et al.,  
78 2015) and Asian scales (Kurokawa et al., 2013; Li et al., 2023a; Li et al., 2017b; Zhang et al., 2009). Researches on establishing  
79 integrated inventories for China are constrained due to the inherent complexity and challenging accessibility of the data. These  
80 efforts are concentrated in specific regions, such as the Yangtze River Delta (YRD) (An et al., 2021).  
81 In this work, with the support of several research institutions, we use an emission integration model to construct a high-  
82 resolution integrated emission inventory at a spatial resolution of  $0.1^\circ$  for China in 2017, denoted as INTAC. The challenges  
83 associated with coupling multi-source heterogeneous data are addressed through the implementation of an inventory  
84 integration framework. Then, leveraging the strengths of inventories enriched with local knowledge, we compile a  
85 comprehensive highly resolved emission product to enhance the accurate representation of emissions from crucial regions,  
86 sectors and species. Finally, the improved accuracy of emission magnitude and spatial distribution is evaluated using  
87 atmospheric chemistry models.

## 88 **2 Methodology and data**

89 Figure 1 illustrates the schematic diagram of the integration process of INTAC. We collect seven emission inventories—MEIC  
90 developed by Tsinghua University (Li et al., 2017a; Zheng et al., 2018), the industrial point source emission inventory for  
91 China by the MEIC team (Zheng et al., 2021; Zheng et al., 2017), the YRD air pollutant emission inventory led by Nanjing  
92 University (An et al., 2021; Zhou et al., 2017b), the Pearl River Delta (PRD) emission inventory by Jinan University (Huang  
93 et al., 2021; Sha et al., 2021), the open biomass burning emission inventory in China by Peking University (Huang et al., 2012a;  
94 Liu et al., 2015b; Song et al., 2009; Yin et al., 2019), the shipping emission inventory in East Asia by Tsinghua University  
95 (Liu et al., 2016b; Liu et al., 2019), and the high-resolution ammonia emission inventory in China (PKU-NH<sub>3</sub>) by Peking  
96 University (Huang et al., 2012b; Kang et al., 2016). The details of these inventories and the rationale for choosing them will  
97 be described in Sect. 2.1.



98 **Figure 1: Methodology framework of the INTAC inventory development.**

99 An integration model is then established to merge together emission inventories with different sectors, species, spatial-temporal  
 100 resolution and formats (i.e., point, area, and gridded forms). The integration process consists of five steps: source mapping,  
 101 species mapping, temporal disaggregation, spatial allocation, and spatial-temporal coupling, as detailed in Sect. 2.2. Based on  
 102 the priority order, multi-source emission inventories are assembled at the standardized species, sector, and grid levels, yielding  
 103 a standardized data cube. Ultimately, the integrated emission inventory INTAC is created for China, featuring a resolution of  
 104 0.1 ° on a monthly scale and covering nine air pollutants (i.e., SO<sub>2</sub>, NO<sub>x</sub>, CO, NMVOC, NH<sub>3</sub>, PM<sub>10</sub>, PM<sub>2.5</sub>, BC, OC).

## 105 2.1 Components of the integrated emission inventory INTAC

106 Table 1 lists the essential details about the seven inventories and priority order utilized for integration. Given MEIC’s extensive  
 107 coverage across species, sectors, and spatial domains, it functions as the default inventory in our integration, supplementing  
 108 the missing data in other inventories. The remaining six inventories can be categorized into three types in sequence: point-  
 109 source-based inventory (ranked sixth), regional inventories (ranked fifth and fourth), and process-based inventories (ranked  
 110 third to first). The point-source-based inventory can directly correct the spatial misallocation of industrial emissions in MEIC  
 111 at fine scales (Zheng et al., 2021; Zheng et al., 2017). The regional inventories further enhance local investigations of individual  
 112 emission sources and simultaneously refine estimation methods for mobile and area sources (Gu et al., 2023; Zhao et al., 2018;  
 113 Zhou et al., 2017b). Process-based inventories typically adopt advanced methods to improve the characterization for emission  
 114 processes and parameters specific to particular sectors or species, thereby providing emission totals and distributions that are  
 115 more in line with measurements (Huang et al., 2012a; Huang et al., 2012b; Kang et al., 2016; Liu et al., 2016b; Liu et al., 2019;  
 116 Liu et al., 2015b; Song et al., 2009; Yin et al., 2019).

117 Table 1: List of emission inventories collected in this work.

Priority ranking	Emission inventory and developer	Year	Resolution	Region	Resolution	Species
1	PKU-NH <sub>3</sub> (Peking University)	1980– 2017	Monthly	Mainland China	0.1 °	NH <sub>3</sub>
2	The shipping emission inventory for East Asia (Tsinghua University)	2017	Annually	East Asia	0.1 °	SO <sub>2</sub> /NO <sub>x</sub> /CO/NMVOC/ PM <sub>2.5</sub> /BC/OC
3	The open biomass burning emission inventory for China (Peking University)	1980– 2017	Daily	Mainland China	~1km	SO <sub>2</sub> /NO <sub>x</sub> /CO/NMVOC/ NH <sub>3</sub> /PM <sub>10</sub> /PM <sub>2.5</sub> /BC/OC
4	The PRD emission inventory (Jinan University)	2017	Monthly	PRD	0.05 °	SO <sub>2</sub> /NO <sub>x</sub> /CO/NMVOC/ NH <sub>3</sub> /PM <sub>10</sub> /PM <sub>2.5</sub> /BC/OC
5	The YRD emission inventory (Nanjing University/Shanghai Academy of Environmental Sciences/Jiangsu Provincial Academy of Environmental Science)	2017	Annually	YRD	0.1 °	SO <sub>2</sub> /NO <sub>x</sub> /CO/NMVOC/ NH <sub>3</sub> /PM <sub>10</sub> /PM <sub>2.5</sub> /BC/OC
6	The industrial point source emission inventory for China (Tsinghua University)	2012– 2018	Monthly	Mainland China	~1km	SO <sub>2</sub> /NO <sub>x</sub> /CO/NMVOC/ NH <sub>3</sub> /PM <sub>10</sub> /PM <sub>2.5</sub> /BC/OC
7	MEICv1.3 (Tsinghua University)	2008– 2017	Monthly	Mainland China	0.25 °	SO <sub>2</sub> /NO <sub>x</sub> /CO/NMVOC/ NH <sub>3</sub> /PM <sub>10</sub> /PM <sub>2.5</sub> /BC/OC

118 **2.1.1 MEIC**

119 The integrated inventory INTAC is built upon MEIC, a comprehensive database with extensive coverage across time periods,  
120 space, species, and sectors. Developed by Tsinghua University since 2010 (<http://meicmodel.org.cn>) (Li et al., 2017a; Zheng  
121 et al., 2018), the MEIC provides monthly emissions for air pollutants and CO<sub>2</sub> in China from 1990 to the present at a resolution  
122 of 0.25 ° × 0.25 °. It caters to the demand for timely and accurate estimates of atmospheric emissions, gaining widespread  
123 adoption by both domestic and international research institutions. We use 2017 emissions from MEIC v1.3 in this study.  
124 MEIC employs several strategies to improve emission estimation parameters. This includes categorizing emission sources  
125 across ~800 sectors, utilizing a technology- and big-data-driven approach for dynamic emission characterization, and

126 employing a localized emission factor database (Li et al., 2017a; Zheng et al., 2018). Emission estimates for power, on-road,  
127 and residential sources are enhanced through the use of unit-level data (Liu et al., 2015a), county-level emission estimates  
128 (Zheng et al., 2014), and integration of extensive household surveys (Peng et al., 2019), respectively. MEIC builds an database  
129 encompassing temporal allocation profiles (ranging from yearly to monthly, daily, and hourly) (Li et al., 2017b), spatial  
130 allocation proxies (from province to county, and further to grids) (Geng et al., 2017; Li et al., 2017b; Zheng et al., 2017), and  
131 a speciation framework for NMVOC involving five mechanisms (CB-IV, CB05, SAPRC-07, SAPRC-99, and RADM2) (Li et  
132 al., 2014) (Li et al., 2014) to support the development of model-ready gridded emissions.  
133 Among the seven inventories, MEIC has the lowest priority, and is only considered when the other six cannot provide necessary  
134 emissions for a specific city and source.

### 135 **2.1.2 The industrial point source emission inventory for China**

136 The proxy-based method used for spatial allocation in MEIC introduces biases in emission mapping, especially at kilometer  
137 scale (Zheng et al., 2021; Zheng et al., 2017). To significantly reduce the uncertainty, we merged an industrial emission  
138 inventory with detailed information on ~100,000 facilities into INTAC.

139 Compiled by Tsinghua University for the year 2013 (Zheng et al., 2021) and updated by the MEIC team for 2017, this point-  
140 based inventory combines three databases investigated under the guidance of the Chinese government, offering a  
141 comprehensive overview of industrial facilities. It includes details on locations, activity rates, production technology, end-of-  
142 pipe pollution control devices, and other parameters. It is worth noting that the facility-level activity data was corrected using  
143 provincial activity data from MEIC as a total constraint to be consistent with national totals from statistics (Zheng et al., 2021).  
144 The facility-level, technology-based approach allows for dynamic tracking of emission fluctuations resulting from  
145 technological advancements and tightening emission regulations. Crucially, the use of facility geolocations rather than relying  
146 on spatial proxies like urban population enables the derivation of gridded industrial data at a resolution of ~1 km. This approach  
147 significantly avoids misallocating emissions from rural to urban areas at fine grids, as supported by previous studies  
148 demonstrating its effectiveness in mitigating simulated biases in air pollutant concentrations within densely populated regions  
149 (Zheng et al., 2021). For temporal variations, it employs the same monthly profiles as MEIC, including the production of  
150 various industrial goods or Gross Domestic Product (GDP), as outlined in Li et al. (2017b). The NMVOC speciation also  
151 aligns with the MEIC model. This inventory takes priority over MEIC, indicating that only few industrial sources not covered  
152 in this inventory are substituted with MEIC.

### 153 **2.1.3 The YRD air pollutant emission inventory**

154 Regional emission inventories in YRD provide a more accurate representation of emissions compared to the national-scale  
155 MEIC, as proven by ground and satellite observations (Yang and Zhao, 2019; Zhang et al., 2021; Zhao et al., 2017a; Zhao et  
156 al., 2018; Zhao et al., 2020; Zhou et al., 2017b). This improvement is attributed to the avoidance of outdated or non-localized  
157 emission calculation parameters, commonly present in large-scale inventories like MEIC. Here, we merge the 2017 YRD air

158 pollutant emission inventory into INTAC for state-of-the-art estimates for rapidly changing emissions over this core area (An  
159 et al., 2021; Gu et al., 2023; Zhou et al., 2017b).  
160 Localized field surveys and measurements greatly enhance the reliability of calculation parameters within the YRD inventory.  
161 Highly-resolved emissions for the power sector are acquired through on-site monitoring with high temporal resolution (Zhang  
162 et al., 2019b), rather than relying on static and outdated average emission factors. Facility-level information (e.g., the removal  
163 efficiencies) obtained from local investigation and a segment-based industrial process method enhances the understanding of  
164 both the quantity and spatial patterns of industrial emissions. Considering meteorological factors and land use conditions  
165 during agricultural processes results in more accurate seasonal and spatial distributions of NH<sub>3</sub> emissions. (Zhao et al., 2020).  
166 An investigation of in-use machinery is conducted to capture the seasonal emission patterns from off-road machines (Zhang  
167 et al., 2020). Real-world surveys are performed to determine grain straw ratios and household burning proportions, facilitating  
168 the quantification of emissions from biomass-fueled stoves. The PM<sub>2.5</sub> and NMVOC speciation profiles are updated based on  
169 multi-instrument sampling and analysis in both current and previous studies (Huang et al., 2018; Zhao et al., 2017a), satisfying  
170 the needs for simulating PM<sub>2.5</sub> chemical components and O<sub>3</sub>. The YRD inventory is collected with a spatial resolution of 0.1  
171 degree and an annually temporal resolution in this study. Only CB05 VOC species are collected.

#### 172 **2.1.4 The PRD emission inventory**

173 The regional emission inventories in the PRD region have demonstrated enhanced reliability compared to previous studies  
174 (Huang et al., 2021; Sha et al., 2021; Zheng et al., 2012). The PRD emission inventory in this study captures spatial and  
175 temporal variations within the PRD region under emission control policies, serving as a foundation for supporting air quality  
176 modeling (Huang et al., 2021; Sha et al., 2021).

177 The PRD inventory exhibits notable accuracy improvements, achieved through big data-driven estimation methods, updated  
178 spatial-temporal allocations, and localized NMVOC speciation profiles. Gridded hourly open biomass burning emissions are  
179 quantified by fusing the fire radiative power data from three satellites, and hourly shipping emissions are estimated using high-  
180 frequency Automatic Identification System (AIS) records. Thirty-one monthly profiles and ten spatial proxies are updated to  
181 reflect spatial-temporal patterns of emissions influenced by economic growth and energy consumption adjustment.  
182 Approximately 90% of industrial emissions are disaggregated using exact locations, and novel proxies (e.g., farmland  
183 production potential) have been developed for several sectors. The NMVOC speciation is carried out through massive localized  
184 measurements and literature reviews, manifested as a collection of 480 NMVOC source profiles across eight sectors and 380  
185 species. The species relevant to the SAPRC-07 chemical mechanism are collected in this work. Additionally, the inventory  
186 encompasses 800 source categories, placing particular emphasis on incorporating new sectors relevant to VOC emissions.  
187 Activity rates are improved through extensive field surveys and data mining efforts, involving investigations of production  
188 data for 10,000 industrial plants and the gathering of activity-relevant information for 50 million vehicles. Emission factors  
189 that reflect local context are obtained or revised based on source measurements and latest research findings. These updates

190 help mitigate uncertainties in emission estimates for the PRD region. The PRD inventory is initially collected at a monthly  
191 resolution and a spatial resolution of 0.05 °, with detailed spatial-temporal allocation proxies outlined in Huang et al. (2021).

### 192 **2.1.5 The open biomass burning emission inventory in China**

193 As a significant source of CO<sub>2</sub>, BC, OC and other pollutants, open biomass burning profoundly influences air quality, climate  
194 change, and human health (Reisen et al., 2013). A case study in summer 2011 for the YRD region revealed that during a severe  
195 haze episode, open biomass burning contributed to 37%, 70%, and 61% of PM<sub>2.5</sub>, OC, and EC emissions, respectively (Cheng  
196 et al., 2014). To address the absence of this source in MEIC, we integrate a high-resolution open biomass burning emission  
197 inventory from Peking University into INTAC (Huang et al., 2012a; Liu et al., 2015b; Song et al., 2009; Yin et al., 2019).  
198 The inventory applies satellite observations to tackle considerable uncertainties tied to provincial statistical data and overcome  
199 the coarse resolution found in previous studies (Ni et al., 2015). The estimation of biomass consumption in the inventory is  
200 based on the fire radiative energy (FRE) approach, which depends on the energy emitted by fires. This approach helps reduce  
201 the biases introduced by burned areas algorithms, especially for small-scale fires. The inventory utilizes the high spatial  
202 resolution land cover dataset GlobeLand30 derived from multispectral images to classify biomass fuel types. Eventually, daily  
203 emissions from forest, grassland, cropland and shrubland are calculated at a 1-kilometer resolution. The reasonableness is  
204 validated by comparing with other datasets, such as the fourth version of the Global Fire Emissions Database. The initially  
205 collected inventory lacks model-ready VOC species.

### 206 **2.1.6 The shipping emission inventory in East Asia**

207 In recent years, maritime trade in the East Asian region has significantly increased (Trade and Development, 2014), resulting  
208 in a surge in shipping emissions with substantial impacts on air quality and climate. Previous studies have indicated that East  
209 Asian shipping emissions accounted for 16% of the global total in 2013. Shipping emissions made a growing contribution to  
210 the rise in annual mean PM<sub>2.5</sub> concentrations, reaching levels as high as 5.2 µg/m<sup>3</sup> in 2015 (Lv et al., 2018). To address the  
211 omission of this emission source in the MEIC, we integrate the shipping emission inventory in East Asian for 2017 into INTAC  
212 (Liu et al., 2016b; Liu et al., 2019).

213 The inventory introduces an innovative approach based on comprehensive and dynamic ship activity data. A static dataset of  
214 approximately 66,000 vessels is compiled as a foundation, using information from Lloyd's Register and China Classification  
215 Society. This dataset encompasses various ship properties, including ship category, hull shape, engine rotational speed, engine  
216 capacity, maximum speed capability, build year, and more. High quality AIS data is used to capture ship activities,  
217 incorporating the Maritime Mobile Service Identification identifier, geographical location, real-time speed, and time-related  
218 information. The AIS data is also employed to generate gridded emissions from shipping at a spatial resolution of 0.1 °. The  
219 inventory enhances our comprehension of regional-level shipping emissions and significantly alleviates biases arising from  
220 the misallocation of marine fuels, as observed in global studies (Endresen et al., 2007). The collected shipping inventory  
221 provides emissions at an annually resolution for seven species, including SO<sub>2</sub>, NO<sub>x</sub>, CO, NMVOC, PM<sub>2.5</sub>, BC, and OC.



### 222 **2.1.7 PKU-NH<sub>3</sub>**

223 As a prominent alkaline component in the atmosphere, ammonia plays a crucial role in atmospheric chemistry, terrestrial and  
224 aquatic ecosystems through its participation in atmospheric reactions and deposition processes. This study integrates PKU-  
225 NH<sub>3</sub>, a high-resolution ammonia emission inventory for China developed by Peking University. PKU-NH<sub>3</sub> is designed to track  
226 the evolution of NH<sub>3</sub> emissions amid the rapid increase in grain and meat production in China over the past few decades  
227 (Huang et al., 2012b; Kang et al., 2016). This inventory offers a better grasp on NH<sub>3</sub> emissions in China through the application  
228 of a processed-based method and more reliable emission factors, in contrast to previous studies (Kurokawa et al., 2013; Li et  
229 al., 2017b). Top-down NH<sub>3</sub> inversion through satellite observations provides additional validation for the accuracy of PKU-  
230 NH<sub>3</sub> (Paulot et al., 2014).

231 Earlier studies of NH<sub>3</sub> emissions commonly used fixed EFs, overlooked some ammonia emission sources, and had coarse  
232 resolutions (Ohara et al., 2007; Streets et al., 2003). Unlike previous approaches, the PKU-NH<sub>3</sub> incorporates dynamic and  
233 multifactorial EFs and more comprehensive emissions sources. The determination of emission factors takes into account  
234 various parameters related to local conditions and agricultural practices. When estimating NH<sub>3</sub> emissions of synthetic fertilizer  
235 application, the model considers five types of fertilizers, as well as factors such as soil acidity, ambient temperature, fertilizer  
236 application technique and dosage, wind speed, and in-situ measurements of NH<sub>3</sub> flux. For livestock waste, NH<sub>3</sub> emissions are  
237 calculated using a mass-flow approach across four phases of manure management, considering variables such as animal rearing  
238 types, temperature and wind speed. In addition, NH<sub>3</sub> emissions from other small sources are also quantified, including  
239 agricultural soil, nitrogen-fixing crop, crop residue compost, excretion of rural populations, open biomass burning, waste  
240 disposal, gasoline vehicles, diesel vehicles, and industrial processes. The NH<sub>3</sub> emissions are allocated from provinces into 0.1 °  
241 grids based on spatial proxies such as land cover, rural population, and other relevant indicators. Monthly emission factors  
242 shaped by meteorological conditions are used to calculate NH<sub>3</sub> emissions from fertilizer application and livestock source at a  
243 monthly level.

## 244 **2.2 The integration of multi-source heterogeneous data**

245 In the integration process, seven heterogeneous inventories are first normalized in terms of emission sources, species, spatial-  
246 temporal resolutions, and then integrated following a priority order to produce a standardized, highly-resolved data cube.

### 247 **2.2.1 Source mapping**

248 To merge inventories under a unified emission source classification system, the emission sources in the MEIC model are  
249 categorized into 88 standard sectors for mapping (Table S1). The first-level category comprises 10 subcategories, namely,  
250 stationary combustion, industrial process, mobile source, solvent use, agriculture, dust, biomass burning, storage and  
251 transportation, waste treatment and other sources. These are then further subdivided into 88 second-level sources, which take  
252 industrial classification for national economic activities for reference. For example, the industrial process sector encompasses

253 emission sources such as the manufacturing of non-metallic mineral products, manufacturing of chemical fibers, manufacturing  
254 of foods, smelting and pressing of ferrous metals, and more. In the initial step of integration, the sectors in each emission  
255 inventory are mapped to the standardized two-level sources.

### 256 **2.2.2 Species mapping**

257 Then, non-methane volatile organic compounds (NMVOC), particulate matter (PM), and  $\text{NO}_x$  in each inventory are converted  
258 into model-ready species to support CTMs. The species mapping process is grounded in the chemical species mapping methods  
259 in MEIC model (Li et al., 2017b; Li et al., 2014). The model supports aerosol chemical schemes such as AER05 and AER06.  
260  $\text{NO}_x$  emissions are allocated to NO and  $\text{NO}_2$  emissions based on ground observations. The step-by-step NMVOC speciation  
261 framework developed in Li et al. (2014) is employed to generate emissions for various gas-phase chemical mechanisms  
262 commonly used in CTMs, including CB-IV, CB05, SAPRC-07, SAPRC-99 and RADM2. The framework incorporates an  
263 explicit assignment approach and updated profiles based on both local measurements and the SPECIATE database v.4.5. The  
264 sources abundant with oxygenated volatile organic compounds (OVOC) are identified, and the incomplete profiles with  
265 missing OVOC fractions are corrected. The accurate speciation mapping helps reduce uncertainties in model-ready emissions.  
266 For inventories providing speciated VOC emissions for certain mechanisms (e.g., the YRD inventory for CB05, PRD inventory  
267 for SAPRC-07), we directly use their emissions, or alternatively, utilize MEIC's speciation framework to generate model  
268 species for the five chemical mechanisms.

### 269 **2.2.3 Temporal disaggregation**

270 The seven emission inventories are collected at different temporal resolutions (Table 1) and need to be temporally allocated to  
271 a unified monthly scale for integration. Monthly emissions from PKU- $\text{NH}_3$ , the PRD inventory, the industrial point source  
272 inventory and MEIC can be directly used for data merge. Daily-level open biomass burning emission inventory for China is  
273 aggregated to monthly scales through summation. For annually inventory (e.g., the YRD inventory), sector-specific monthly  
274 profiles derived from the MEIC model are used for disaggregation (Li et al., 2017b). For instance, monthly power generation  
275 data from the National Bureau of Statistics describe variations in monthly power emissions. Industrial production or GDP from  
276 the National Bureau of Statistics are employed to account for monthly emission fluctuations related to industrial heating,  
277 boilers, cement, iron and steel, and other industrial processes. Monthly emission factors calculated by the International Vehicle  
278 Emissions model are applied to on-road vehicles. Considering the insignificant monthly variations of Automatic Identification  
279 System data for marine shipping, the annual shipping emissions are uniformly disaggregated across the months.

### 280 **2.2.4 Spatial allocation**

281 The seven inventories are in different data formats, including point source and gridded formats at varying resolutions,  
282 necessitating spatial harmonization for integration. Although the industrial point source inventory and the open biomass  
283 burning inventory can accurately pinpoint the specific geographic locations of emission sources, the other five inventories rely

284 on numerous spatial proxies to disaggregate emissions into grids, which inevitably introduce uncertainties at very fine  
285 resolutions. Therefore, we re-grid the final product to 0.1 ° to ensure high level spatial accuracy. Gridded emissions finer than  
286 0.1 ° resolution are aggregated to 0.1 °, which is performed in the open biomass burning inventory and the PRD inventory. For  
287 the industrial point source inventory, latitude and longitude coordinates are employed to directly position them within grid  
288 locations. Area sources in MEIC are allocated to grids using spatial proxies within the MEIC model (Li et al., 2017b). For  
289 instance, industrial sources are assigned to grids based on urban population (Schneider et al., 2009). The road network (Zheng  
290 et al., 2014) serves as a proxy for disaggregating emissions of on-road vehicles, while rural population (Schneider et al., 2009)  
291 is used as the proxy for fertilizer and livestock sources. It's important to mention that uncertainties may arise at city borders if  
292 emissions from adjacent cities come from different inventories during the integration process. To mitigate biases introduced  
293 by border issues, all emissions at 0.1 ° resolution are first uniformly downscaled to 1 km for the spatial-temporal coupling  
294 process, and then re-gridded back to 0.1 ° for the final product.

### 295 **2.2.5 Spatial-temporal coupling**

296 Finally, following the procedures outlined in Sections 2.2.1 to 2.2.4, all inventories are preprocessed to a standardized format,  
297 encompassing 88 sectors, various species, a spatial resolution of 1 km, and a monthly temporal resolution. This preprocessing  
298 prepares the inventories for merging, ultimately resulting in the generation of a standardized data cube.  
299 The integration is carried out at source-by-source, species-by-species, and grid-by-grid levels, with the process guided by the  
300 priority order of each inventory (Table 1). MEIC serves as the default inventory in our integration, offering extensive spatial  
301 and species coverage, along with spatial proxies, temporal profiles, and NMVOC speciation methods within the model. The  
302 remaining six emission inventories are assigned a predefined priority order. The industrial point source emission inventory for  
303 China takes precedence over industrial emissions in MEIC, substituting proxy-based spatial allocation with precise  
304 geographical coordinates. This extends the applicability of MEIC from a resolution greater than 0.25 ° to finer scale (Zheng et  
305 al., 2021; Zheng et al., 2017). To achieve fine-grained emission characterization in critical areas, the YRD and PRD emission  
306 inventory enriched with localized data and advanced methods are incorporated to update emissions in these areas. While MEIC  
307 comprehensively estimates emissions for ~800 source categories in China, there may still be omissions for certain emission  
308 sources. The inclusion of inventories for open biomass burning and East Asian shipping helps partially fill this gap. The PKU-  
309 NH<sub>3</sub>, generated by a process-based model to provide a comprehensive understanding of China's NH<sub>3</sub> sources, is utilized to  
310 replace all NH<sub>3</sub> emissions in other inventories. The prioritization is performed city by city. For emissions of a particular species  
311 from a specific emission sector, when multiple inventories overlap in city grids, the estimates from the highest-priority  
312 inventory is selected as the final emissions. Through this step, the integrated inventories are developed based on the configured  
313 output settings, such as map projection and spatial-temporal attributes.

### 314 **2.3 Evaluation of the emission inventory using WRF/CMAQ model**

315 We apply Weather Research and Forecasting Version 3.9 (WRFv3.9) and Community Multiscale Air Quality Version 5.2  
316 (CMAQ5.2) as the air quality simulation systems. Two nested simulation domains with horizontal resolutions of 36 and 12  
317 km are used (Fig. S1). The mother domain ( $172 \times 127$  cells) covers the entire China and parts of the neighboring countries,  
318 and the nested domain ( $226 \times 241$  cells) includes the heavily polluted Eastern China. Four-month (January, April, July, and  
319 October) simulations in 2017 is carried out, with a 7-day spin-up period preceded each month. The vertical resolution in WRF  
320 is set with 45 sigma levels ranging from the surface up to 100 hPa. Subsequently, it is collapsed into 28 layers through the  
321 Meteorology-Chemistry Interface Processor (MCIP) before being input into CMAQ.

322 The configuration of WRF and CMAQ model in this study follows Cheng et al. (2019). The meteorological initial and boundary  
323 conditions for the simulation are provided by the final reanalysis data from the National Centers for Environmental Prediction  
324 (NCEP-FNL, <https://rda.ucar.edu/datasets/ds083.2/>). The schemes for shortwave radiation, longwave radiation, land surface  
325 processes, boundary layer, cumulus parameterization, and cloud microphysics are selected as the New Goddard scheme (Chou  
326 et al., 1998), RRTM scheme (Mlawer et al., 1997), Pleim–Xiu surface layer scheme (Xiu and Pleim, 2001), ACM2 PLB  
327 scheme (Pleim, 2007), Kain-Fritsch scheme (Kain, 2004), and WSM6 scheme (Hong and Lim, 2006), respectively.  
328 Observational nudging and soil nudging are employed to enhance the meteorological simulation. Regarding CMAQ model,  
329 the chemical mechanisms for gas-phase, aqueous-phase, and aerosol are configured as CB05, the Regional Acid Deposition  
330 Model (RADM), and AERO6, respectively. Photolysis rates are calculated online using the simulated aerosols and ozone  
331 concentrations. Anthropogenic emissions outside China are taken from MIX inventory (Li et al., 2017b). The integrated  
332 inventory INTAC and MEIC are used for comparison within China. Biogenic emissions are calculated using the Model of  
333 Emissions of Gases and Aerosols from Nature version 2.1 (MEGANv2.1), while dust and lightning emissions are not  
334 considered in this study.

335 The performances of WRF for the meteorological parameters are evaluated against the Integrated Surface Database (ISD) from  
336 the National Climatic Data Center (NCDC) of the National Climate Data Center (<ftp://ftp.ncdc.noaa.gov/pub/data/noaa/>).  
337 Evaluation metrics include correlation coefficient (R), mean bias (MB), root mean square error (RMSE), normalized mean  
338 bias (NMB), and normalized mean error (NME). Table S2 demonstrates good agreement between WRF model results and  
339 ground-level observations. Similar configurations have been also validated in previous studies (Cheng et al., 2019; Cheng et  
340 al., 2021a; Cheng et al., 2021b). CMAQ modeling results are assessed using hourly observed concentrations of air pollutants  
341 obtained from the China National Environmental Monitoring Center (<http://www.cnemc.cn/>).

## 342 **3 Results**

### 343 **3.1 China's emission characteristics in 2017**

344 We utilized the integrated emission inventory to analyze pollutant emissions in China for the year 2017. Major air pollutant  
345 emissions were estimated as follows: 12.3 Tg SO<sub>2</sub>, 24.5 Tg NO<sub>x</sub>, 141.0 Tg CO, 27.9 Tg NMVOC, 9.2 Tg NH<sub>3</sub>, 11.1 Tg PM<sub>10</sub>,  
346 8.4 Tg PM<sub>2.5</sub>, 1.3 Tg BC, and 2.2 Tg OC. The emission data, organized into power, industry, residential, transportation,  
347 agriculture, solvent use, shipping, and open biomass burning sectors, are available for download from  
348 <https://doi.org/10.5281/zenodo.10459198> (Wu et al., 2024) and <http://meicmodel.org.cn/intac>. The following sections will  
349 characterize emissions in detail across sectors, fuel types, and spatial distributions.

#### 350 **3.1.1 By sectors**

351 Table 2 displays emissions specific to power, industry, residential, transportation, agriculture, solvent use, shipping, and open  
352 biomass burning sectors in the integrated emission inventory INTAC. For pollutants primarily originating from fuel  
353 combustion and industrial processes (e.g., SO<sub>2</sub>, NO<sub>x</sub>, CO, PM<sub>10</sub>, and PM<sub>2.5</sub>), the power, industry, and transportation sources  
354 make a significant contribution to their emissions, ranging from 56% to 83%. Industrial sources take a leading role in various  
355 atmospheric pollutants, contributing more than 30% for SO<sub>2</sub>, NO<sub>x</sub>, CO, NMVOC, PM<sub>10</sub>, and PM<sub>2.5</sub> emissions. Due to low  
356 combustion efficiency and a lack of emission control measures, residential sources exhibit a high emission factor for products  
357 of incomplete combustion, leading to 40% of CO emissions, 48% for BC, and 73% for OC. Solvent sources exclusively  
358 produce NMVOC emissions, constituting 33% to the overall emissions. The complexity of VOC emission origins is evident  
359 in the diverse range of contributing sources. Agricultural sources dominate NH<sub>3</sub> emissions, comprising an 83% share of total  
360 emissions. As described in Sect. 2.1.7, the PKU-NH<sub>3</sub> incorporates a wide variety of NH<sub>3</sub> sources, providing a more  
361 comprehensive understanding of the sectors contributing to NH<sub>3</sub> emissions. Insignificant sources may exert large influence in  
362 specific regions or periods, such as during large wildfires or in cities with heavy traffic. Additionally, the contribution of the  
363 supplemented open biomass burning source cannot be overlooked, especially for OC (7%) and NMVOC (6%).

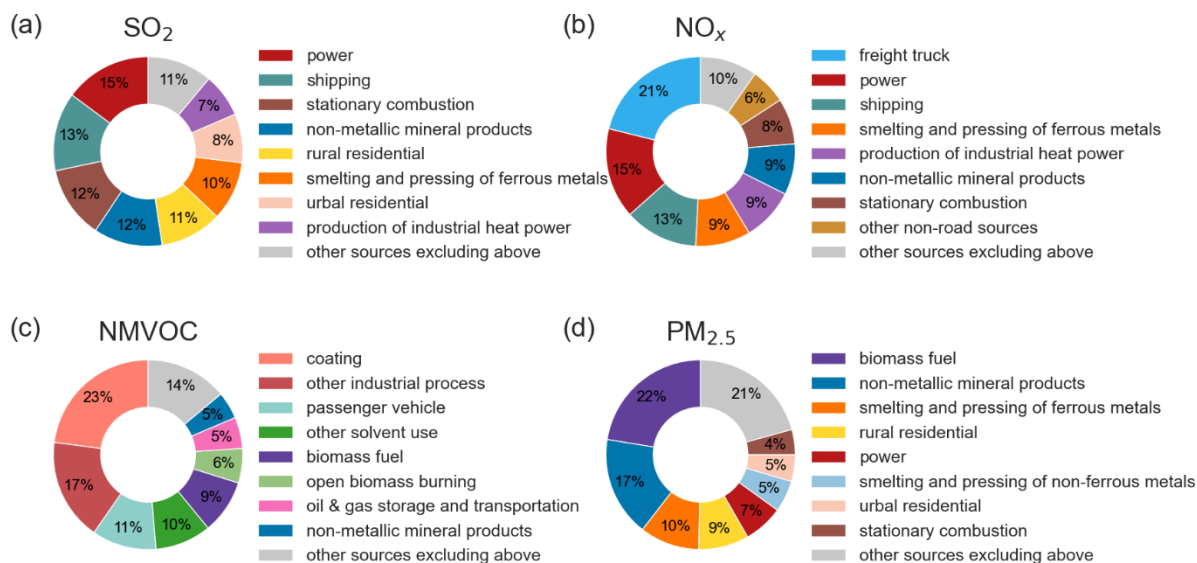
364 Figure 2 consolidates 88 standardized emission sources into 25 categories, allowing for a more detailed analysis of sectoral  
365 emission patterns compared to Table 2. Owing to substantial coal use in industrial and power sectors, along with sulfur-rich  
366 ship fuels, prominent contributors to SO<sub>2</sub> emissions include power, shipping, stationary combustion, and manufacture of non-  
367 metallic mineral products sources, accounting for 15%, 13%, 12%, and 12% respectively to total SO<sub>2</sub> emissions. This indicates  
368 that achieving further reductions in SO<sub>2</sub> emissions will require the implementation of more energy-efficient, end-of-pipe  
369 control measures, and adoption of low-sulfur fuels. The dominant origins of NO<sub>x</sub> emissions are from the freight truck, power  
370 generation, and shipping sectors, representing 21%, 15%, and 13% of the total emissions. Both freight trucks and vessels  
371 extensively use compression ignition engines, prone to generating NO<sub>x</sub> emissions under high-temperature and oxygen-rich  
372 conditions. Implementing strict vehicle standards is crucial to effectively reduce NO<sub>x</sub> emissions from exhaust gases. Coatings,  
373 other industrial processes, and passenger vehicle sources constitute 51% of anthropogenic NMVOC emissions. The major

374 contributors to primary PM<sub>2.5</sub> emissions include biomass fuel, the manufacture of non-metallic mineral products, and the  
 375 smelting and pressing of ferrous metals source, making up 22%, 17%, and 10% of the total emissions, respectively. It's  
 376 noteworthy that the use of biomass fuels (e.g., rice straw, firewood) for cooking or heating in rural areas results in considerable  
 377 PM<sub>2.5</sub> emissions, especially in provinces like Sichuan, Anhui, Shandong, and Heilongjiang.

378

379 **Table 2: Anthropogenic emissions of air pollutants by sectors in the 2017 INTAC inventory for China (Units: Gg).**

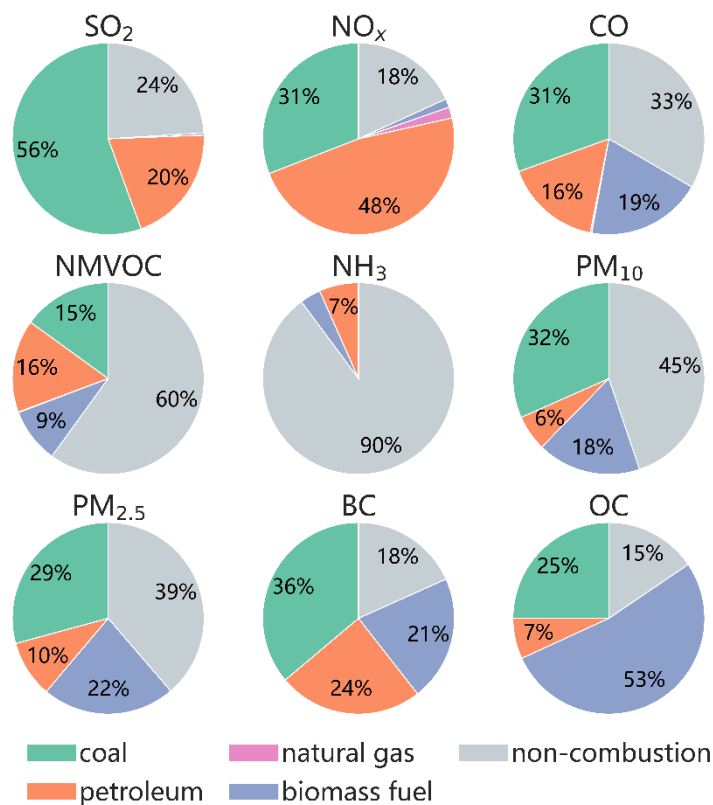
Sectors	SO <sub>2</sub>	NO <sub>x</sub>	CO	NMVOC	NH <sub>3</sub>	PM <sub>10</sub>	PM <sub>2.5</sub>	BC	OC
<b>Power</b>	1822	3790	4909	152	14	981	568	6	0
<b>Industry</b>	6066	8800	52828	8824	249	5603	3620	308	285
<b>Residential</b>	2361	861	55895	3676	629	3516	3088	606	1649
<b>Transportation</b>	341	7751	22597	4123	619	533	493	257	95
<b>Agriculture</b>	0	0	0	0	7609	0	0	0	0
<b>Solvent</b>	0	0	0	9255	0	0	0	0	0
<b>Shipping</b>	1642	3077	391	191	2	73	264	43	49
<b>Open biomass burning</b>	21	215	4403	1659	76	409	355	35	167
<b>Total</b>	12253	24494	141023	27881	9198	11117	8388	1255	2245



380 **Figure 2: Sector-specific distributions of emissions in the 2017 INTAC inventory for China.** (a), (b), (c) and (d) represent the sectoral  
 381 contributions for SO<sub>2</sub>, NO<sub>x</sub>, NMVOC and PM<sub>2.5</sub>, respectively. The figure only displays the top eight contributing sources, while sources  
 382 excluding these are categorized as "other sources".

### 383 3.1.2 By fuel types

384 Figure 3 illustrates the proportions of major air pollutant emissions in 2017 for each fuel type. Fossil fuel combustion  
 385 significantly dominates the emissions of PM<sub>10</sub>, PM<sub>2.5</sub>, CO, BC, SO<sub>2</sub>, NO<sub>x</sub>, with proportion ranging from 38% to 80%. The coal  
 386 combustion accounts for 56% of SO<sub>2</sub> emissions, with power, residential activities and industrial production as the primary  
 387 emitter. Meanwhile, petroleum combustion, mainly from marine vessels, constitutes 20% of SO<sub>2</sub> emissions. For NO<sub>x</sub> emissions,  
 388 petroleum combustion contributes 48% of the total, predominantly arising from freight trucks (5.2 Tg), marine vessels (3.1  
 389 Tg), and passenger vehicles (1.0 Tg). Coal combustion processes, such as power (3.6 Tg) and industrial boiler (2.2 Tg) also  
 390 result in substantial NO<sub>x</sub> emissions (31%). The biomass fuel source causes 53% of OC emissions. Emissions of NMVOC and  
 391 NH<sub>3</sub> are primarily associated with non-combustion processes.

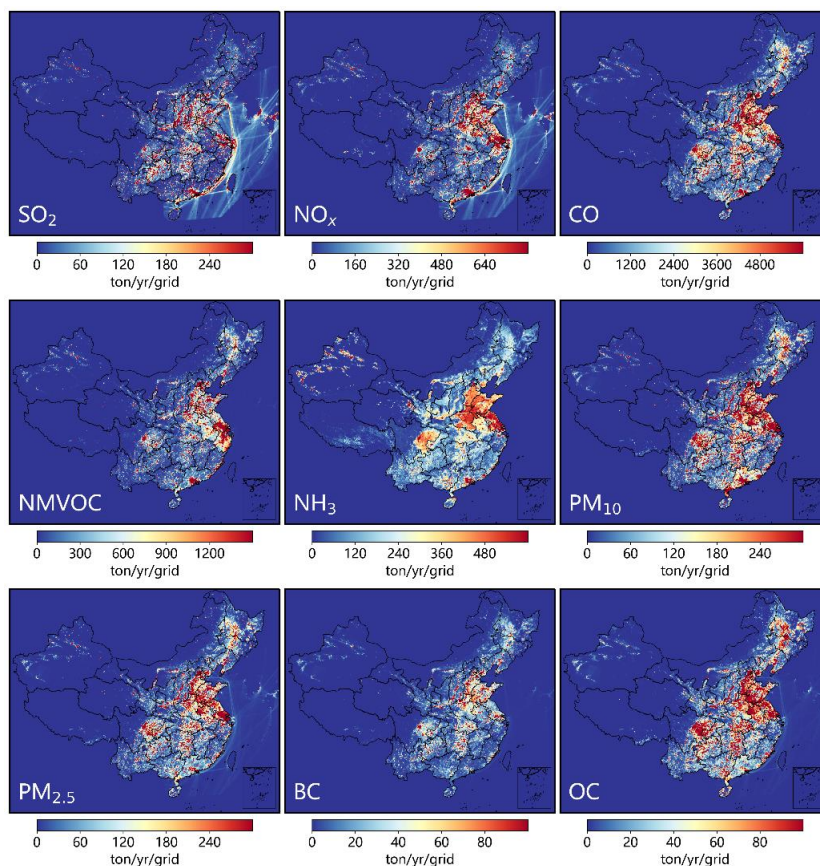


392 **Figure 3: Fuel-specific distributions of major air pollutant emissions in the 2017 INTAC inventory for China.**

### 393 3.1.3 Spatial distribution

394 We present the gridded emission maps of major air pollutants in Fig. 4. Emissions from anthropogenic sources in China exhibit  
 395 significant spatial heterogeneity. Due to economic growth and industrial activities, air pollutant emissions are primarily  
 396 concentrated in the central and eastern regions of China, especially in economically developed urban clusters such as the  
 397 Beijing-Tianjin-Hebei (BTH) region, the YRD, the PRD, as well as in regions like Sichuan and Chongqing. These four key

398 areas, as depicted in Fig. S2, collectively account for 26%, 34%, 35%, 37%, 35%, 33%, 27%, 27%, and 29% of the national  
399 emissions of SO<sub>2</sub>, NO<sub>x</sub>, CO, NMVOC, NH<sub>3</sub>, PM<sub>10</sub>, PM<sub>2.5</sub>, BC, and OC, respectively. Moreover, the emission maps at a fine  
400 spatial resolution of 0.1° × 0.1° present the local variations in emission patterns, identifying numerous hotspots in small areas  
401 and showcasing distinct gradients in emissions. Table 3 shows the provincial-level emissions (except Hong Kong, Macao, and  
402 Taiwan), and a map depicting provincial boundaries is displayed in Fig. S2. The emission levels in specific provinces are  
403 determined by factors such as resource endowments, industrial structure, energy consumption, and emission control measures.  
404 Taking SO<sub>2</sub> as an example, the top five provinces are Shanxi, Shandong, Hebei, Guizhou, and Inner Mongolia, collectively  
405 accounting for 36% of the national total SO<sub>2</sub> emissions. The Guizhou Province, located in the southwest of China, is  
406 characterized by high-sulfur coal and a relatively gradual implementation of pollution control measures, which results in  
407 elevated SO<sub>2</sub> emissions. In other four provinces, large scale heavy industries have led to substantial coal consumption and  
408 correspondingly higher SO<sub>2</sub> emissions. Provinces with a less industry-focused economic structure and lower energy  
409 consumption, including Tianjin, Hainan, Qinghai, Beijing, and Tibet, exhibit the lowest SO<sub>2</sub> emissions, accounting for  
410 approximately 2% of the national total.



411 **Figure 4: Spatial distributions of major air pollutant emissions in the 2017 INTAC inventory for China.**



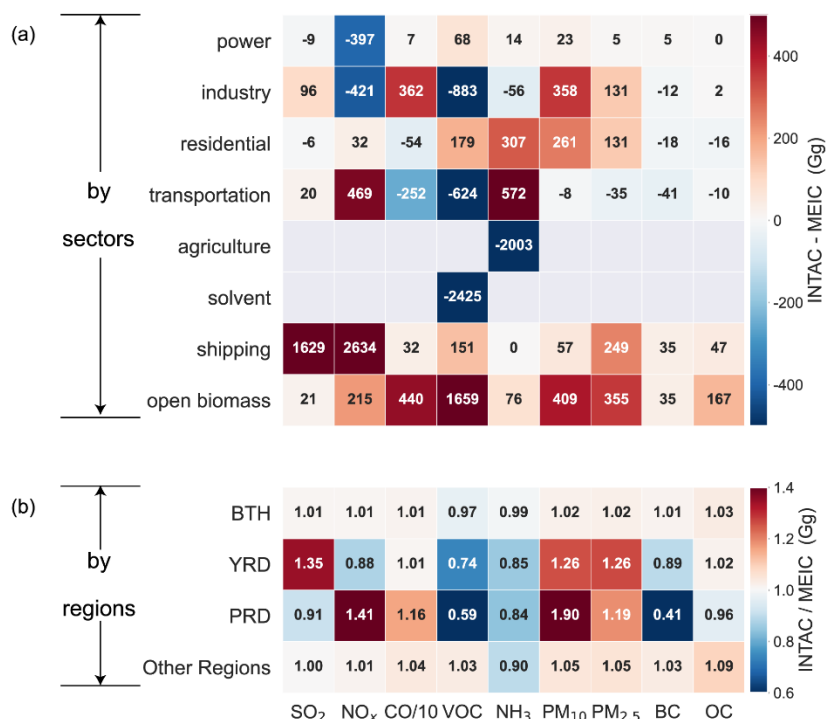
412 **Table 3: Anthropogenic emissions of air pollutants by provinces in the 2017 INTAC inventory for China (Units: Gg).** The shipping  
 413 emission inventory in East Asia is not included.

<b>Sectors</b>	<b>SO<sub>2</sub></b>	<b>NO<sub>x</sub></b>	<b>CO</b>	<b>NM VOC</b>	<b>NH<sub>3</sub></b>	<b>PM<sub>10</sub></b>	<b>PM<sub>2.5</sub></b>	<b>BC</b>	<b>OC</b>
<b>Anhui</b>	319	850	5968	1094	340	603	447	50	116
<b>Beijing</b>	27	232	1397	519	36	62	50	7	16
<b>Chongqing</b>	401	377	2424	566	149	210	160	22	48
<b>Fujian</b>	162	532	2349	899	149	204	153	22	49
<b>Gansu</b>	191	353	2225	359	276	165	127	22	42
<b>Guangdong</b>	435	1573	6912	1274	351	793	359	17	68
<b>Guangxi</b>	268	436	3586	811	323	359	277	29	84
<b>Guizhou</b>	660	357	6643	510	236	464	350	76	127
<b>Hainan</b>	48	95	586	172	57	47	37	5	15
<b>Hebei</b>	675	1704	11756	1681	522	717	532	88	126
<b>Heilongjiang</b>	249	825	7049	1426	378	501	407	65	158
<b>Henan</b>	371	1262	7979	1507	677	628	463	79	109
<b>Hubei</b>	519	706	6355	1188	357	461	357	68	119
<b>Hunan</b>	524	635	6817	958	329	487	366	77	123
<b>Inner Mongolia</b>	601	1217	5760	834	561	465	343	56	90
<b>Jiangsu</b>	395	1222	8646	1536	497	675	500	50	106
<b>Jiangxi</b>	181	451	3684	649	209	277	197	28	53
<b>Jilin</b>	238	655	3982	851	207	310	240	39	77
<b>Liaoning</b>	464	1205	5848	1322	268	437	328	54	88
<b>Ningxia</b>	228	329	767	179	79	92	63	7	9
<b>Qinghai</b>	44	107	599	130	131	60	45	5	8
<b>Shaanxi</b>	338	551	3789	824	273	297	223	39	69
<b>Shandong</b>	957	2144	11494	2859	694	907	684	105	152
<b>Shanghai</b>	116	471	1133	344	29	106	87	16	6
<b>Shanxi</b>	989	968	6030	759	199	561	419	64	82
<b>Sichuan</b>	384	781	6375	1485	644	468	374	56	143
<b>Tianjin</b>	91	335	1437	575	33	82	62	9	12
<b>Xinjiang</b>	260	610	2645	635	515	220	160	23	32
<b>Xizang</b>	1	52	150	46	149	15	12	2	5
<b>Yunnan</b>	335	437	3831	579	397	305	232	38	76
<b>Zhejiang</b>	297	672	3016	1348	118	274	197	23	22

414 **3.2 Improved accuracy of China’s anthropogenic emissions by INTAC**

415 **3.2.1 Comparison of emission magnitudes in INTAC with MEIC across sectors and regions**

416 The INTAC inventory improves the representation of anthropogenic air pollutant emissions by incorporating a large number  
 417 of industrial point sources, integrating high-resolution regional inventories, and supplementing missing emission sources in  
 418 MEIC. Remarkable differences between INTAC and MEIC are illustrated in Fig. 5 across regions and sectors. Compared to  
 419 MEIC, the INTAC inventory shows higher level of 16.7%, 11.5%, 10.8%, 11.0%, and 9.1% for SO<sub>2</sub>, NO<sub>x</sub>, PM<sub>10</sub>, PM<sub>2.5</sub>, and  
 420 OC emissions, respectively. However, it indicates lower levels of 6.3% and 10.6% for NMVOC and NH<sub>3</sub>. CO and BC  
 421 emissions exhibit good agreement between the two inventories, with differences lower than 3.9%. In comparison to MEIC, the  
 422 supplementary emission sources in INTAC—specifically, open biomass burning and marine shipping—account for the  
 423 majority of increased emissions, contributing 95%, 89%, and 74% for SO<sub>2</sub>, CO, and PM<sub>2.5</sub>, respectively. Additionally, the  
 424 incorporation of PKU-NH<sub>3</sub> in INTAC leads to a 21% decrease in NH<sub>3</sub> emissions from agricultural sources, while NH<sub>3</sub>  
 425 emissions from residential sources and transportation increase by 99% and 13.1 times, respectively. Such difference in  
 426 agricultural sources is mainly caused by the estimates of synthetic fertilizer (Kang et al., 2016), particularly concerning the  
 427 treatment of fertilizer types and corresponding emission factors.

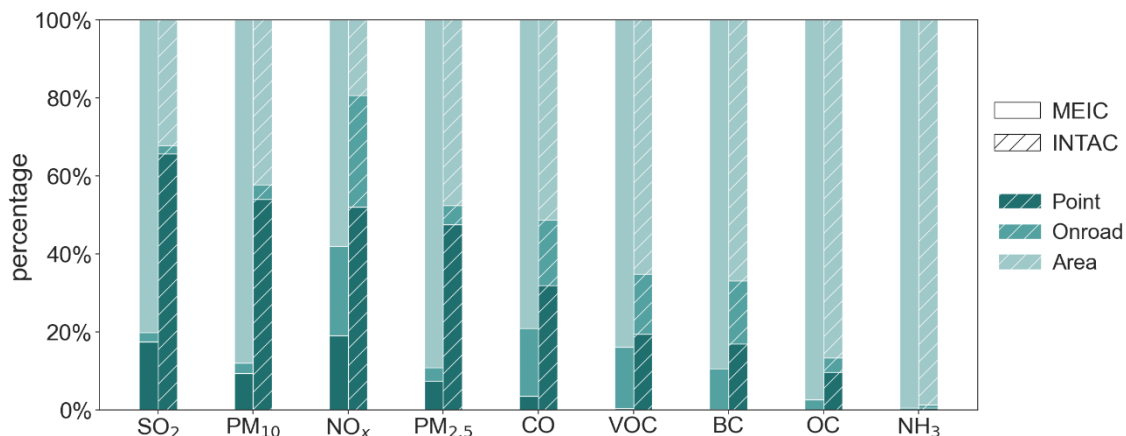


428 **Figure 5: Inter-comparisons of emission estimates between the INTAC inventory and MEIC.** (a) shows the difference by sectors, and  
 429 (b) presents the ratio of emissions in INTAC to those in MEIC.

430 Many discrepancies between MEIC and INTAC arise from the integration of regional emission inventories. As presented in  
431 Fig. 5b, notable disparities are observed in the YRD and PRD region. Estimates for NO<sub>x</sub> emissions in the YRD region are  
432 approximately 88% of those derived from the MEIC model. This highlights an enhanced precision attributable to reliable  
433 assessments of denitrification efficiency in power plants and the measured NO<sub>x</sub> emission factors for both power plants and  
434 boilers within the integrated YRD inventory, as supported by previous research studies (Zhao et al., 2018). INTAC's estimates  
435 for NMVOC emissions from the YRD region are 26% lower than estimates in MEIC. The overestimation in MEIC mainly  
436 results from the uncertainties of solvent use source, particularly coating and printing and dyeing processes. The integrated  
437 YRD emission inventory employs more accurate calculation parameters, such as statistical data from local city yearbooks,  
438 industry association reports, and apparent consumption of solvents. Furthermore, the speciation profiles of NMVOC are  
439 localized and corrected based on the literature research and measurements. In the PRD region, The NO<sub>x</sub> emissions from INTAC  
440 are 41% higher than MEIC estimates, with non-road sources and non-metallic mineral products contributing 45% and 40% to  
441 this difference, respectively. The PRD inventory employs a detailed calculation approach for shipping emissions based on AIS  
442 data, in contrast to the simplified approach for inland waterway sources in MEIC. The NO<sub>x</sub> emissions from industrial processes  
443 of brick and flat glass manufacturing are not considered in MEIC, which is a deficiency that is addressed in the integrated PRD  
444 inventory. INTAC's NMVOC emissions are approximately 59% of those from MEIC. The disparity is particularly notable in  
445 industrial and solvent use sources, contributing 49% and 35%, respectively, to the observed difference. In INTAC, nearly half  
446 of the VOC emission factors for industrial solvent sources are based on local measurements, and a preference for raw material-  
447 based calculations over product-based ones reduces uncertainty in the estimation. For significant VOC-emitting sources like  
448 cleaning solvents, MEIC employs an emission factor of 1000 g/kg, whereas the PRD inventory uses 850 g/kg. In the case of  
449 oil refineries, the emission factors are 2.76 g/kg for MEIC and 1.82 g/kg for the PRD inventory.

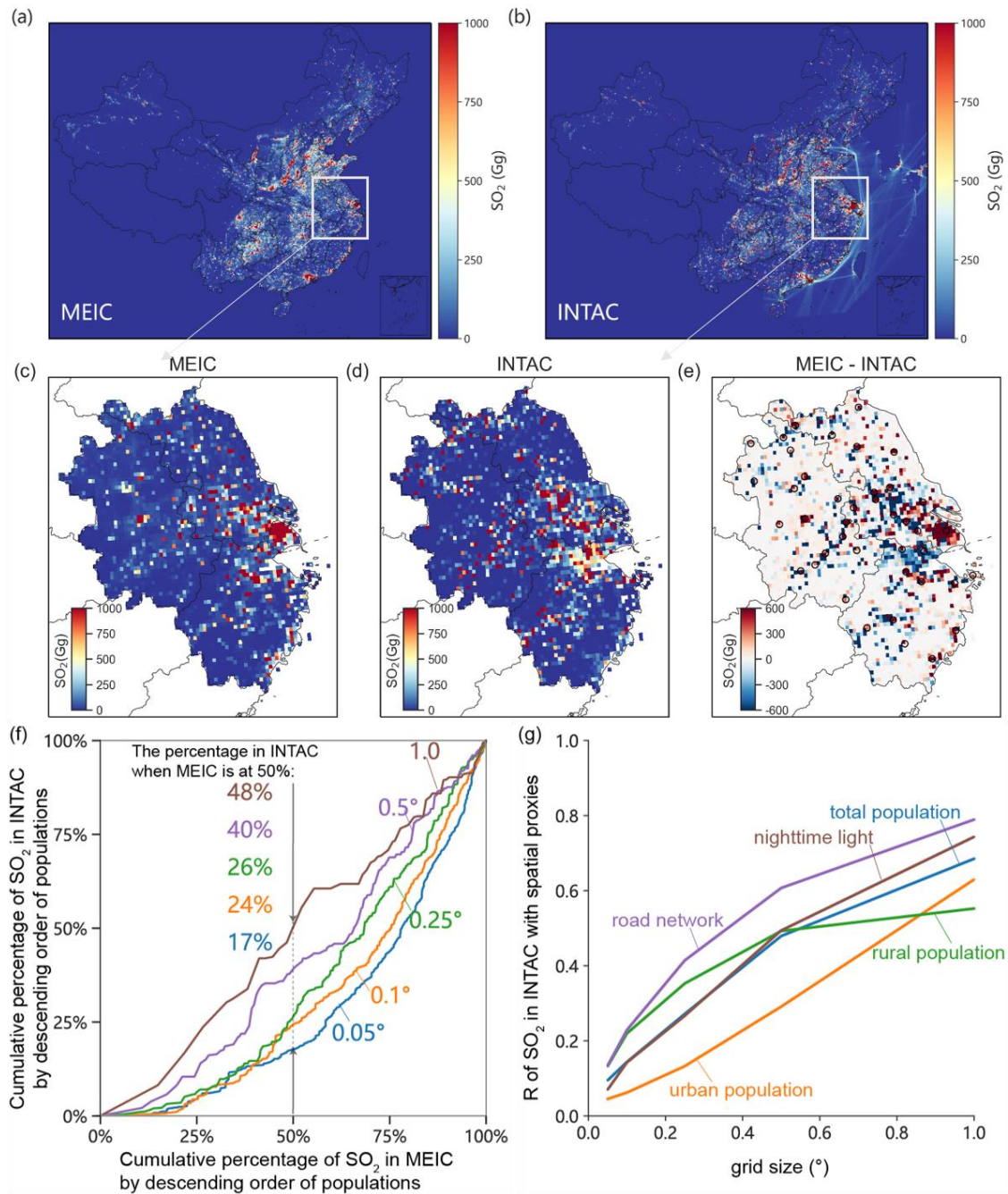
### 450 **3.2.2 Impact of point source contributions**

451 The most accurate method for obtaining emissions at finer-scale grids relies on spatial allocation based on precise geographical  
452 coordinates. In MEIC, the majority of emission sources are represented as area sources and distributed onto grids using spatial  
453 proxies such as urban population, except for power plants. In contrast, the increased proportion of industrial point source  
454 emissions in INTAC significantly constrains the uncertainties associated with spatial proxies. Figure 6 shows the inter-  
455 comparisons of percentage of point, on-road, and area source emissions between the INTAC and MEIC. Air pollutants,  
456 especially those dominated by industrial combustion sources like SO<sub>2</sub>, NO<sub>x</sub>, PM<sub>10</sub>, and PM<sub>2.5</sub>, exhibit a significantly higher  
457 proportion of point source emissions within INTAC compared to MEIC. In MEIC, the proportion of point source emissions  
458 for SO<sub>2</sub>, PM<sub>10</sub>, NO<sub>x</sub>, and PM<sub>2.5</sub> is 17%, 9%, 19%, and 7%, respectively. However, in the INTAC inventory, these percentages  
459 substantially increase to 66%, 54%, 52%, and 48%, respectively, indicating a more accurate representation of spatial patterns.  
460 For other species with emissions mainly from area sources (e.g., residential and transportation), there are limited improvements  
461 in the proportion of point source emissions in INTAC.



462 **Figure 6: Inter-comparisons of percentage of point, on-road, and area source emissions between the INTAC inventory and MEIC.**

463 To further assess the impact arising from point sources, Figure 7 takes SO<sub>2</sub> and YRD region as an example to compare the  
 464 spatial emission patterns between INTAC and MEIC. Figures 7c–e reveal that MEIC tends to overestimate emissions in urban  
 465 centers and underestimate emissions in rural areas compared to INTAC. Amid economic growth and rapid urbanization,  
 466 MEIC’s use of urban population as a proxy for spatial allocation becomes impractical as many factories relocate from city  
 467 centers to rural areas. To elucidate the difference between population-based and point-source-based allocation methods in  
 468 emissions mapping, we present the cumulative percentage of SO<sub>2</sub> emissions in MEIC and INTAC based on descending  
 469 population orders in Fig. 7f. We use the grid groups where densely populated areas contribute 50% of SO<sub>2</sub> emissions in MEIC  
 470 as an example, comparing them with the cumulative percentage in INTAC across various grid sizes. The results indicate that  
 471 at a resolution of 0.05 °, INTAC only accounts for 17% of the emissions, while it reaches to 48% as the grid size increases to  
 472 1.0 °. This suggests that at a fine grid scale, MEIC tends to allocate more emissions to densely populated urban areas, while  
 473 INTAC allocates a larger proportion to suburban and rural areas, aligning better with the real-world emission spatial patterns.  
 474 This mitigation of bias through INTAC is especially notable at finer resolutions. The close cumulative percentage at 1.0 ° in  
 475 the two inventories can be attributed to the fact that urban and suburban areas often fall within the same grid, leading to a  
 476 decreasing enhancement in spatial accuracy achieved by INTAC. Figure 7g further presents the correlation between the spatial  
 477 patterns of SO<sub>2</sub> emissions in INTAC and various spatial proxies. At a resolution of 1.0 °, the correlation coefficients between  
 478 emission distributions and factors (i.e., road networks, nighttime lights, total population, urban population, and rural population)  
 479 fall within the range of 0.55 to 0.79. Nevertheless, at a resolution of 0.05 °, the correlation coefficients range from 0.05 to 0.13.  
 480 This indicates that at higher spatial resolutions, INTAC substantially reduces the bias introduced by spatial proxies in MEIC.



481 **Figure 7: Spatial pattern analysis of emissions in the INTAC inventory, using SO<sub>2</sub> emissions as an example.** (a) and (b) display the  
 482 spatial distributions of SO<sub>2</sub> emissions in MEIC and INTAC, respectively. MEIC emissions have been downscaled from 0.25 degrees to 0.1  
 483 degrees for comparison. To compare MEIC and INTAC in details, a zoom-in is applied to the YRD region. (c), (d), and (e) show spatial  
 484 distributions of SO<sub>2</sub> emissions in MEIC, INTAC and their difference. Circles in (e) represent the center of a city. (f) compares cumulative  
 485 percentage of SO<sub>2</sub> emissions in the INTAC inventory with those in MEIC across different spatial resolutions. The gridded SO<sub>2</sub> emissions,  
 486 ranging from resolutions of 0.05 ° to 1.0 °, are cumulated in descending order of populations. The percentage annotations in different colors  
 487 indicate the level of accumulated SO<sub>2</sub> emissions in INTAC at various spatial resolutions when SO<sub>2</sub> emissions in MEIC reach 50%

488 accumulation. (g) shows correlation coefficient between SO<sub>2</sub> emissions in the INTAC inventory and multiple spatial proxies at different grid  
489 sizes.

### 490 3.3 Improvements on air quality modelling by INTAC

#### 491 3.3.1 Overall performance in key regions

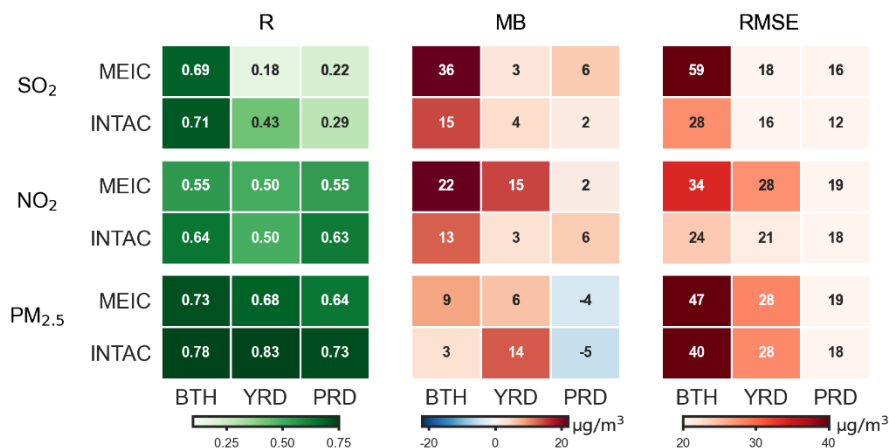
492 We conduct simulations using the WRF-CMAQ model driven by INTAC and MEIC separately to evaluate the improvements  
493 in modeled air pollutant concentrations. Table 4 evaluates the simulated emissions in 74 major cities (locations depicted in Fig.  
494 S2) against in-situ observations, with corresponding scatter plots shown in Fig. S3. The INTAC demonstrates an improved  
495 agreement between modeled concentrations and ground-level observations, which benefits from the integrated high resolution  
496 inventories. Compared to MEIC, INTAC leads to a decline in the mean bias of simulated major pollutant concentrations by 2–  
497 14 µg/m<sup>3</sup>, a reduction in the root mean square error by 4–19 µg/m<sup>3</sup>, and a decrease in the normalized mean error by 4–71%.  
498 This finding indicates that INTAC produces a more accurate characterization of emissions in China overall. Furthermore,  
499 given that atmospheric pollution monitoring stations are mainly located in urban areas in China, the observed differences  
500 suggest that the INTAC can mitigate the overestimation of major pollutant concentrations in urban centers. As discussed in  
501 Sect. 3.2.2, MEIC overestimates emissions in urban areas and underestimates them in rural and suburban areas, consequently  
502 introducing uncertainties into air quality modeling. The improved accuracy in spatial distributions within INTAC significantly  
503 contributes to enhancing the overall accuracy of air pollutant modeling.

504 **Table 4: The discrepancies between simulated SO<sub>2</sub>, NO<sub>2</sub> and PM<sub>2.5</sub> concentrations and observed values for 74 major cities at a**  
505 **resolution of 12 km, using MEIC and INTAC as emission inputs.** The statistical metrics used for comparison include R, MB, and RMSE.  
506 The bold font represents the difference of modeling performance between INTAC and MEIC.

Pollutants	Inventory	MB (µg/m <sup>3</sup> )	RMSE (µg/m <sup>3</sup> )	NME (%)
SO <sub>2</sub>	INTAC	11	30	92
	MEIC	25	49	163
	<b>Difference</b>	<b>-14</b>	<b>-19</b>	<b>-71</b>
NO <sub>2</sub>	INTAC	7	22	43
	MEIC	18	31	60
	<b>Difference</b>	<b>-11</b>	<b>-9</b>	<b>-17</b>
PM <sub>2.5</sub>	INTAC	6	35	46
	MEIC	8	39	50
	<b>Difference</b>	<b>-2</b>	<b>-4</b>	<b>-4</b>

507 Figure 8 further compares the overall simulation performance between INTAC and MEIC in three key regions (BTH, YRD,  
508 and PRD), with corresponding scatter plots shown from Fig. S4 to S6. Regarding PM<sub>2.5</sub> and its precursors, MEIC shows a  
509 considerable mean bias of up to 36 µg/m<sup>3</sup> and a root mean square error of up to 59 µg/m<sup>3</sup> in key regions. In contrast, INTAC

510 demonstrates the maximum MB values of 15  $\mu\text{g}/\text{m}^3$  and RMSE values of 40  $\mu\text{g}/\text{m}^3$ . The correlation coefficients between  
 511 simulated and observed concentrations of the three air pollutants are generally lower in MEIC compared to those in INTAC.  
 512 The modeling performance driven by INTAC, particularly for short-lived pollutants, experiences significant improvement due  
 513 to their strong correlation with spatial distributions of emission sources. Nonetheless, discrepancies between modeled and  
 514 observed surface concentrations still exist because of uncertainties from meteorological, physical, and chemical processes  
 515 within chemical transport models. Moreover, emission sources such as residential, transportation, agriculture in INTAC are  
 516 treated as nonpoint sources, and their allocation to grids using spatial proxies can introduce biases to air quality modeling. It  
 517 is noteworthy that simulated ammonium concentrations by INTAC agree better with ground measurements than MEIC (Table  
 518 S3). While  $\text{NH}_4^+$  concentrations are influenced by secondary chemical reactions, the improved model performance still reflects  
 519 the benefits from the integration of PKU- $\text{NH}_3$ .



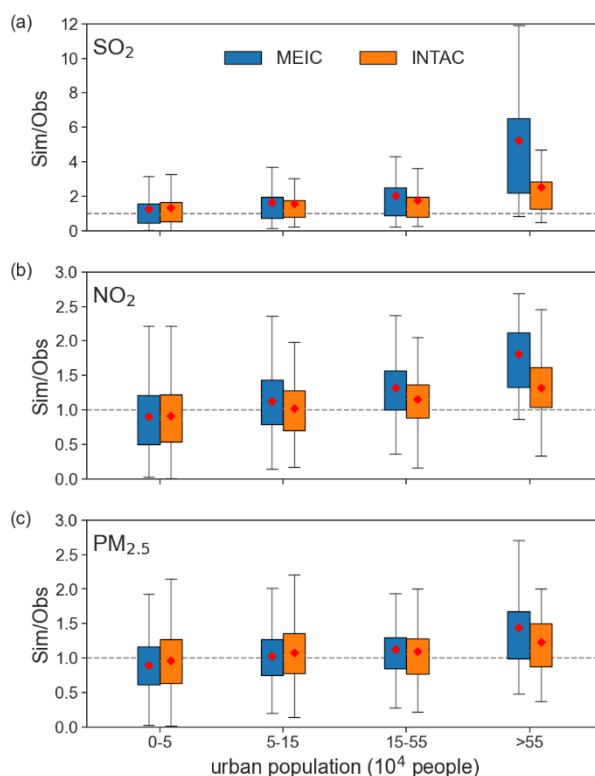
520 **Figure 8: The Comparison of modeling performance across key regions (i.e., BTH, YRD, PRD) when using MEIC and INTAC as**  
 521 **emission inputs, respectively.** The statistical metrics used for comparison include R, MB, and RMSE. The regions under comparison  
 522 comprise the BTH, YRD, and PRD.

### 523 3.3.2 Improvements across different spatial resolutions

524 To provide a more in-depth assessment of improved spatial patterns in INTAC, Figure 9 categorizes grid cells into different  
 525 bins based on their urban population and calculates the ratio of simulated pollutant concentrations to ground observations for  
 526 both INTAC and MEIC in each category. The results demonstrate that as urban population increases, the enhanced model  
 527 performance of INTAC over MEIC for SO<sub>2</sub>, NO<sub>2</sub> and PM<sub>2.5</sub> becomes more evident. Specifically, when the urban population  
 528 is less than 50,000, both INTAC and MEIC exhibit a median range of simulated-to-observed concentration ratios close to 1.  
 529 However, as the urban population exceeds 550,000, the average range for MEIC widens to 1.4–5.2, whereas it remains within  
 530 the range of 0.9–1.0 for INTAC. This indicates a significant improvement in mitigating the overestimation of emissions in  
 531 densely populated areas by INTAC. This indicates that the overestimation of emissions in densely populated areas, caused by  
 532 proxy-based methods in MEIC, introduces uncertainties into chemical transport models. The incorporation of the industrial

533 point source emission inventory for China, along with the YRD and PRD emission inventory significantly increases point  
534 source shares in INTAC, and thus producing better spatial representations for real-world emission distributions and smaller  
535 simulated deviations.

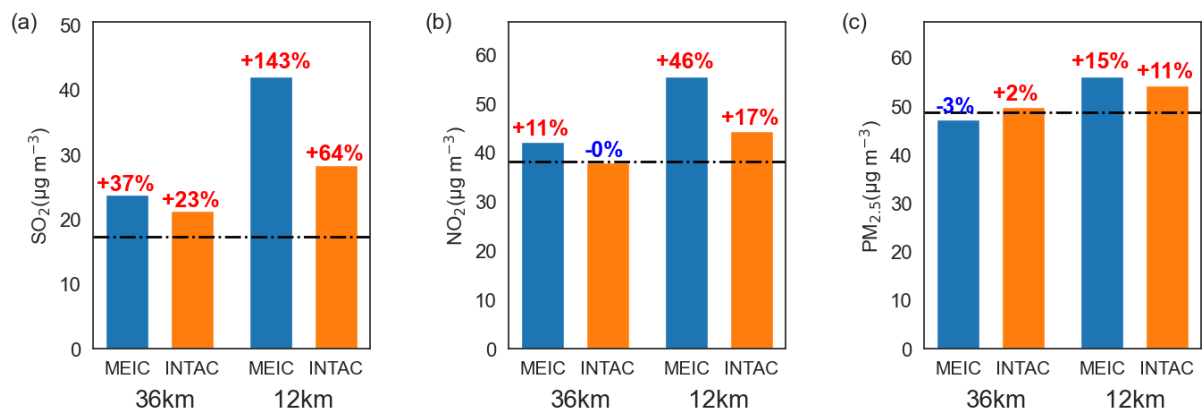
536 Model performance differences between MEIC and INTAC are influenced by grid size. Figure 10 presents the comparison  
537 between modeled  $\text{SO}_2$ ,  $\text{NO}_2$  and  $\text{PM}_{2.5}$  concentrations against ground observations for 74 major cities at resolutions of 36 and  
538 12 km. "Increasing spatial resolution does not lead to a reduction in simulation errors, especially for MEIC. As the horizontal  
539 resolution increases from 36 km to 12 km, the mean biases of simulated  $\text{SO}_2$ ,  $\text{NO}_2$ , and  $\text{PM}_{2.5}$  concentrations using MEIC show  
540 an increase from 37% to 143%, 11% to 46%, and -3% to 15%, respectively, when compared to in-situ observations. In contrast,  
541 the simulation results using INTAC exhibit better agreement with ground observations, with mean biases for  $\text{SO}_2$ ,  $\text{NO}_2$ , and  
542  $\text{PM}_{2.5}$  increasing from 23% to 64%, -0% to 17%, and 2% to 11%, respectively. This is due to the fact that the deviations in  
543 finer grid cells, whether overestimated or underestimated, tend to cancel out at a coarse spatial resolution. The decoupling  
544 between emission spatial distributions with proxies at finer grids leads to more noticeable biases in air quality modeling.  
545 Therefore, the findings suggest that the INTAC developed in this study can effectively constrain uncertainties in emissions  
546 and the modeling bias, especially at fine spatial scales. The improvement will help tackle emerging challenges in high-  
547 resolution air quality modeling in China.



548 **Figure 9: Comparisons of modeling performance between INTAC and MEIC in different ranges of urban population.** The 12 km  
549 grids are categorized to different bins according to the urban population residing within each grid. The ratio of simulated pollutant



550 concentrations (Sim) to observed concentrations (Obs) for major pollutants (SO<sub>2</sub>, NO<sub>2</sub>, and PM<sub>2.5</sub>) are calculated. The boxplot presents the  
 551 upper quartile, median (red dot), and lower quartile of the ratios.



552 **Figure 10: The comparison of modeled air pollutant concentrations and ground observations for 74 cities at 36 and 12 km resolutions,**  
 553 **using MEIC and INTAC as emission inputs, respectively.** The black dashed line represents the observational mean, and the annotations  
 554 above the bar charts indicate the mean biases between simulated concentrations and the corresponding observed value.

#### 555 4 Discussion

556 Qualitative or quantitative uncertainty assessment is a necessary element of a complete inventory for policy or scientific  
 557 purposes. Approaches such as error propagation and Monte Carlo simulation are commonly used for quantitative uncertainty  
 558 analysis in China's emission inventory (Lu et al., 2011; Streets et al., 2003; Zhao et al., 2011; Zhao et al., 2017b). However,  
 559 this study uses an integrated method rather than a unified framework to compile a comprehensive high resolution emission  
 560 inventory for China. Collecting only emission quantities from the seven inventories without detailed calculation parameters  
 561 makes it challenging to assess the overall uncertainties of INTAC here. We have summarized the estimated uncertainty range  
 562 for components of INTAC in Table 5, where such information is available. Although the uncertainties might be reported for a  
 563 year other than 2017, they still provide a rough representation of the uncertainty range in major air pollutant emission estimates  
 564 within INTAC. Species such as SO<sub>2</sub> and NO<sub>x</sub> exhibit relatively low uncertainties, benefiting from well-established estimates  
 565 for large-scale combustion sources. The considerable uncertainties observed in BC and OC emissions may be attributed to  
 566 inaccuracies in the emission factors of the residential sector. Further details regarding the uncertainties of each component  
 567 inventory can be found in corresponding literature (An et al., 2021; Huang et al., 2021; Kang et al., 2016; Liu et al., 2016b;  
 568 Yin et al., 2019; Zhao et al., 2011).

569 The uncertainties of INTAC also arise from the integrated process: (1) The emission source categories are based on the MEIC  
 570 model, and sectors in other inventories need to be mapped to the 88 standard sectors first. Due to limited foundational  
 571 information for an aggregated sector's disaggregation, this process may introduce biases for those who initially provide coarser  
 572 source categories. For example, if an inventory only offers one aggregated sector for power, which needs to be broken down  
 573 into four subsectors (i.e., production of power, supply of power, production of industrial heat power and production of

574 residential heat power). We use the energy consumption for corresponding sectors from the statistical yearbook as a reference  
575 basis for this allocation, which is a relatively reliable method despite potential deviations. (2) To generate speciated VOC  
576 species, sectoral NMVOC emissions in each inventory need to be matched to corresponding source profiles from the MEIC  
577 model. Discrepancies in emission source mapping can impact the outcomes, which will be overcome by gathering more  
578 detailed sectoral information for each inventory or directly collecting speciated species in future studies. (3) The INTAC is  
579 made publicly available at a monthly scale, given that the majority of its components are gathered on a monthly or annual  
580 scale. The temporal disaggregation to finer resolutions for modeling is achieved using empirically selected weighting factors  
581 in the MEIC model. However, it is noteworthy that the parameters employed for allocating emissions to daily or hourly scales  
582 remain fixed and do not vary over time or region, introducing additional uncertainties. In the future, we plan to incorporate  
583 more advanced data or method (e.g., real-time emission measurements) to enhance temporal accuracy at finer scales, as  
584 indicated in the previous work for the power sector (Wu et al., 2022). (4) The border issue is inevitable when emissions for the  
585 same species in two adjacent cities are derived from different inventories. A typical example is the cities located at the boundary  
586 of the YRD or the PRD regions. In the INTAC, we downscale all emissions to 1 km before spatial-temporal coupling process,  
587 thereby mitigating this uncertainty to some extent.

588 **Table 5: Uncertainties in the inventory components of INTAC, contingent upon the availability of such information (Unit: %).**

<b>Emission inventory</b>	<b>Reporting year</b>	<b>SO<sub>2</sub></b>	<b>NO<sub>x</sub></b>	<b>CO</b>	<b>NMVOC</b>	<b>NH<sub>3</sub></b>	<b>PM<sub>10</sub></b>	<b>PM<sub>2.5</sub></b>	<b>BC</b>	<b>OC</b>	<b>References</b>
PKU-NH <sub>3</sub>	2012					-26– 25					(Kang et al., 2016)
The shipping emission inventory for East Asia	2013	±4	±4	±5	±4			±4	±4	±4	(Liu et al., 2016b)
The open biomass burning emission inventory for China	2003– 2017	-67– 67	-78– 98	-54– 56		-44– 89	-74– 84	-65– 65	-75– 100	-74– 81	(Yin et al., 2019)
The PRD emission inventory	2017	-17– 20	-25– 28	-30– 39	-34–50	-50– 86	-45– 60	-43– 62	-53– 116	-54– 160	(Huang et al., 2021)
The YRD air pollutant emission inventory	2017	-29– 36	-28– 33	-42– 75	-44–68	-58– 117	-36– 62	-30– 46			(An et al., 2021)
	2005	-14– 13	-13– 37				-14– 45	-17– 54	-25– 136	-40– 121	(Zhao et al., 2011)

589 The INTAC for 2017 is subject to some limitations: (1) The integrated method yields emissions data across various sectors  
590 from different datasets for the same city and species, or emissions in different species from different datasets for the same city  
591 and sector. The utilization of species ratios requires careful consideration in these cases. (2) Limited resources present a  
592 substantial challenge in gathering emission inventories over extended time series from diverse research institutions within the  
593 scope of this study. Consequently, we exclusively present the INTAC for the year 2017, with the possibility of extension to  
594 other years in subsequent research.

## 595 **5 Data Availability**

596 Data described in this manuscript can be accessed at Zenodo under <https://doi.org/10.5281/zenodo.10459198> (Wu et al., 2024)  
597 and <http://meicmodel.org.cn/intac>.

## 598 **6 Concluding remarks**

599 Compiling a comprehensive bottom-up emission inventory for China that encompasses both extensive coverage and high  
600 resolution poses a significant challenge. In this work, we construct a 0.1 °resolution integrated inventory for 2017 through the  
601 fusion of multi-source emission inventories. An integration model has been developed to effectively couple heterogeneous  
602 emission datasets, aimed at generating a standardized data cube with consistent sectors, species, and spatial-temporal resolution.  
603 The INTAC is created through source mapping, species mapping, temporal disaggregation, spatial allocation and spatial-  
604 temporal coupling. Six representative emission inventories focusing on national and regional scales, as well as key species and  
605 sources in China are merged with MEIC. This integration harnesses the strengths of each inventory, resulting in an improved  
606 depiction of emission totals and spatial distribution patterns for China.

607 We find that the total emissions of SO<sub>2</sub>, NO<sub>x</sub>, CO, NMVOC, NH<sub>3</sub>, PM<sub>10</sub>, PM<sub>2.5</sub>, BC, and OC in INTAC for 2017 are 12.3, 24.5,  
608 141.0, 27.9, 9.2, 11.1, 8.4, 1.3 and 2.2 Tg, respectively. Industrial production serves as the main source of various atmospheric  
609 pollutants. Residential sources contribute over 40% to CO, BC and OC emissions. Apart from agricultural sources, which  
610 account for 83% of NH<sub>3</sub> emissions, the contributions from various minor emission sources cannot be overlooked. This study  
611 emphasizes the significance of shipping emissions, particularly in contributing to SO<sub>2</sub> (13%) and NO<sub>x</sub> (13%). Fossil fuel  
612 combustion dominates the emissions of PM<sub>10</sub>, PM<sub>2.5</sub>, CO, BC, SO<sub>2</sub>, and NO<sub>x</sub>, ranging from 38% to 80%. The enhancement in  
613 emission estimates for China in INTAC is demonstrated by the comparison with MEIC. For instance, the incorporation of  
614 numerous point sources has notably addressed MEIC's tendency to overestimate emissions in urban centers, particularly at  
615 higher spatial resolutions. In comparison to MEIC, INTAC exhibits a mean bias reduction in simulated concentrations of major  
616 pollutants against ground observations across 74 cities, ranging from 2–14 µg/m<sup>3</sup>. The improvement in model performance  
617 achieved by INTAC is particularly noticeable at finer spatial resolutions.

618 Our study offers an efficient framework for creating highly-resolved emission inventory on a large scale. This approach  
619 integrates advantages from previous studies and holds the potential to support policymakers in making well-informed decisions  
620 for improving air quality. In the future, we anticipate the ongoing incorporation of additional emission datasets to offer a more  
621 reliable representation of emissions in China over extended time periods.

## 622 **Supplement**

623 The supplement related to this article has six figures and three tables.

## 624 **Author contributions**

625 Nana Wu, Guannan Geng and Qiang Zhang designed the study. Nana Wu developed the INTAC emission inventory and  
626 conducted chemical transport modeling. Junyu Zheng, Yu Song, Huan Liu, Yu Zhao, Ying Zhou and Qinren Shi provided the  
627 emission inventories for the integration. Ruochong Xu helped with the data analysis. Shigan Liu compiled the chemical  
628 transport model. Xiaodong Liu contributed to the design of computer programmes for the integration model. The manuscript  
629 was written by Nana Wu and Guannan Geng, and it was revised and discussed by all coauthors.

## 630 **Competing interests**

631 The authors declare that they have no conflict of interest.

## 632 **Acknowledgements**

633 This work was supported by the National Natural Science Foundation of China (Grant No. 92044303), the National Key R&D  
634 program of China (Grant No. 2022YFC3700605), and the Major Project of High Resolution Earth Observation System (Grant  
635 No. 30-Y60B01-9003-22/23). We thank Zhijiong Huang, Junchi Wang, Mingxu Liu, Wenling Liao, Chen Gu for their  
636 contributions to the handling and transfer of the emission inventories for the integration.

## 637 **References**

638 An, J., Huang, Y., Huang, C., Wang, X., Yan, R., Wang, Q., Wang, H., Jing, S., Zhang, Y., Liu, Y., Chen, Y., Xu, C., Qiao, L., Zhou, M.,  
639 Zhu, S., Hu, Q., Lu, J., and Chen, C.: Emission inventory of air pollutants and chemical speciation for specific anthropogenic sources based  
640 on local measurements in the Yangtze River Delta region, China, *Atmos. Chem. Phys.*, 21, 2003-2025, 10.5194/acp-21-2003-2021, 2021.  
641 Bo, X., Jia, M., Xue, X., Tang, L., Mi, Z., Wang, S., Cui, W., Chang, X., Ruan, J., Dong, G., Zhou, B., and Davis, S. J.: Effect of strengthened  
642 standards on Chinese ironmaking and steelmaking emissions, *Nature Sustainability*, 4, 811-820, 10.1038/s41893-021-00736-0, 2021.  
643 Chen, H., Huang, Y., Shen, H., Chen, Y., Ru, M., Chen, Y., Lin, N., Su, S., Zhuo, S., Zhong, Q., Wang, X., Liu, J., Li, B., and Tao, S.:  
644 Modeling temporal variations in global residential energy consumption and pollutant emissions, *Applied Energy*, 184, 820-829,  
645 <https://doi.org/10.1016/j.apenergy.2015.10.185>, 2016.

646 Cheng, J., Su, J., Cui, T., Li, X., Dong, X., Sun, F., Yang, Y., Tong, D., Zheng, Y., Li, Y., Li, J., Zhang, Q., and He, K.: Dominant role of  
647 emission reduction in PM<sub>2.5</sub> air quality improvement in Beijing during 2013–2017: a model-based decomposition analysis, *Atmos. Chem.*  
648 *Phys.*, 19, 6125–6146, 10.5194/acp-19-6125-2019, 2019.

649 Cheng, J., Tong, D., Liu, Y., Bo, Y., Zheng, B., Geng, G., He, K., and Zhang, Q.: Air quality and health benefits of China's current and  
650 upcoming clean air policies, *Faraday Discussions*, 226, 584–606, 10.1039/D0FD00090F, 2021a.

651 Cheng, J., Tong, D., Liu, Y., Yu, S., Yan, L., Zheng, B., Geng, G., He, K., and Zhang, Q.: Comparison of Current and Future PM<sub>2.5</sub> Air  
652 Quality in China Under CMIP6 and DPEC Emission Scenarios, *Geophysical Research Letters*, 48, e2021GL093197,  
653 <https://doi.org/10.1029/2021GL093197>, 2021b.

654 Cheng, Z., Wang, S., Fu, X., Watson, J. G., Jiang, J., Fu, Q., Chen, C., Xu, B., Yu, J., Chow, J. C., and Hao, J.: Impact of biomass burning  
655 on haze pollution in the Yangtze River delta, China: a case study in summer 2011, *Atmos. Chem. Phys.*, 14, 4573–4585, 10.5194/acp-14-  
656 4573-2014, 2014.

657 Chou, M.-D., Suarez, M. J., Ho, C.-H., Yan, M. M. H., and Lee, K.-T.: Parameterizations for Cloud Overlapping and Shortwave Single-  
658 Scattering Properties for Use in General Circulation and Cloud Ensemble Models, *Journal of Climate*, 11, 202–214, 10.1175/1520-  
659 0442(1998)011<0202:PFCOAS>2.0.CO;2, 1998.

660 Crippa, M., Guizzardi, D., Butler, T., Keating, T., Wu, R., Kaminski, J., Kuenen, J., Kurokawa, J., Chatani, S., Morikawa, T., Pouliot, G.,  
661 Racine, J., Moran, M. D., Klimont, Z., Manseau, P. M., Mashayekhi, R., Henderson, B. H., Smith, S. J., Suchyta, H., Muntean, M., Solazzo,  
662 E., Banja, M., Schaaf, E., Pagani, F., Woo, J. H., Kim, J., Monforti-Ferrario, F., Pisoni, E., Zhang, J., Niemi, D., Sassi, M., Ansari, T., and  
663 Foley, K.: The HTAP\_v3 emission mosaic: merging regional and global monthly emissions (2000–2018) to support air quality modelling  
664 and policies, *Earth Syst. Sci. Data*, 15, 2667–2694, 10.5194/essd-15-2667-2023, 2023.

665 Deng, F., Lv, Z., Qi, L., Wang, X., Shi, M., and Liu, H.: A big data approach to improving the vehicle emission inventory in China, *Nature*  
666 *Communications*, 11, 2801, 10.1038/s41467-020-16579-w, 2020.

667 Endresen, Ø., Sørgeård, E., Behrens, H. L., Brett, P. O., and Isaksen, I. S. A.: A historical reconstruction of ships' fuel consumption and  
668 emissions, *Journal of Geophysical Research: Atmospheres*, 112, <https://doi.org/10.1029/2006JD007630>, 2007.

669 Geng, G., Zhang, Q., Martin, R. V., Lin, J., Huo, H., Zheng, B., Wang, S., and He, K.: Impact of spatial proxies on the representation of  
670 bottom-up emission inventories: A satellite-based analysis, *Atmospheric Chemistry and Physics*, 17, 4131–4145, 2017.

671 Geng, G., Zheng, Y., Zhang, Q., Xue, T., Zhao, H., Tong, D., Zheng, B., Li, M., Liu, F., Hong, C., He, K., and Davis, S. J.: Drivers of PM<sub>2.5</sub>  
672 air pollution deaths in China 2002–2017, *Nature Geoscience*, 10.1038/s41561-021-00792-3, 2021.

673 Gu, C., Zhang, L., Xu, Z., Xia, S., Wang, Y., Li, L., Wang, Z., Zhao, Q., Wang, H., and Zhao, Y.: High-resolution regional emission inventory  
674 contributes to the evaluation of policy effectiveness: a case study in Jiangsu Province, China, *Atmos. Chem. Phys.*, 23, 4247–4269,  
675 10.5194/acp-23-4247-2023, 2023.

676 Hong, S. Y. and Lim, J.-O. J.: The WRF Single-Moment 6-Class Microphysics Scheme (WSM6), *Asia-pacific Journal of Atmospheric*  
677 *Sciences*, 42, 129–151, 2006.

678 Huang, C., Hu, Q., Wang, H., Qiao, L., Jing, S. a., Wang, H., Zhou, M., Zhu, S., Ma, Y., Lou, S., Li, L., Tao, S., Li, Y., and Lou, D.:  
679 Emission factors of particulate and gaseous compounds from a large cargo vessel operated under real-world conditions, *Environmental*  
680 *Pollution*, 242, 667–674, <https://doi.org/10.1016/j.envpol.2018.07.036>, 2018.

681 Huang, X., Li, M., Li, J., and Song, Y.: A high-resolution emission inventory of crop burning in fields in China based on MODIS Thermal  
682 Anomalies/Fire products, *Atmospheric Environment*, 50, 9–15, <https://doi.org/10.1016/j.atmosenv.2012.01.017>, 2012a.

683 Huang, X., Song, Y., Li, M., Li, J., Huo, Q., Cai, X., Zhu, T., Hu, M., and Zhang, H.: A high-resolution ammonia emission inventory in  
684 China, *Global Biogeochemical Cycles*, 26, GB1030, 2012b.

685 Huang, Z., Zhong, Z., Sha, Q., Xu, Y., Zhang, Z., Wu, L., Wang, Y., Zhang, L., Cui, X., Tang, M., Shi, B., Zheng, C., Li, Z., Hu, M., Bi, L.,  
686 Zheng, J., and Yan, M.: An updated model-ready emission inventory for Guangdong Province by incorporating big data and mapping onto  
687 multiple chemical mechanisms, *Science of The Total Environment*, 769, 144535, <https://doi.org/10.1016/j.scitotenv.2020.144535>, 2021.

688 Janssens-Maenhout, G., Crippa, M., Guizzardi, D., Dentener, F., Muntean, M., Pouliot, G., Keating, T., Zhang, Q., Kurokawa, J.,  
689 Wankmüller, R., Denier van der Gon, H., Kuenen, J. J. P., Klimont, Z., Frost, G., Darras, S., Koffi, B., and Li, M.: HTAP\_v2.2: a mosaic of  
690 regional and global emission grid maps for 2008 and 2010 to study hemispheric transport of air pollution, *Atmos. Chem. Phys.*, 15, 11411-  
691 11432, 10.5194/acp-15-11411-2015, 2015.

692 Kain, J. S.: The Kain–Fritsch Convective Parameterization: An Update, *Journal of Applied Meteorology*, 43, 170–181, 10.1175/1520-  
693 0450(2004)043<0170:TKCPAU>2.0.CO;2, 2004.

694 Kang, Y., Liu, M., Song, Y., Huang, X., Yao, H., Cai, X., Zhang, H., Kang, L., Liu, X., Yan, X., He, H., Zhang, Q., Shao, M., and Zhu, T.:  
695 High-resolution ammonia emissions inventories in China from 1980 to 2012, *Atmos. Chem. Phys.*, 16, 2043–2058, 10.5194/acp-16-2043-  
696 2016, 2016.

697 Kurokawa, J., Ohara, T., Morikawa, T., Hanayama, S., Janssens-Maenhout, G., Fukui, T., Kawashima, K., and Akimoto, H.: Emissions of  
698 air pollutants and greenhouse gases over Asian regions during 2000–2008: Regional Emission inventory in ASia (REAS) version 2,  
699 *Atmospheric Chemistry and Physics*, 13, 21(2013-11-13), 13, 2013.

700 Li, B., Chen, L., Shen, W., Jin, J., Wang, T., Wang, P., Yang, Y., and Liao, H.: Improved gridded ammonia emission inventory in China,  
701 *Atmos. Chem. Phys.*, 21, 15883–15900, 10.5194/acp-21-15883-2021, 2021.

702 Li, M., Kurokawa, J., Zhang, Q., Woo, J. H., Morikawa, T., Chatani, S., Lu, Z., Song, Y., Geng, G., Hu, H., Kim, J., Cooper, O. R., and  
703 McDonald, B. C.: MIXv2: a long-term mosaic emission inventory for Asia (2010-2017), *EGU*sphere, 2023, 1-45, 10.5194/egusphere-2023-  
704 2283, 2023a.

705 Li, M., Liu, H., Geng, G., Hong, C., Liu, F., Song, Y., Tong, D., Zheng, B., Cui, H., Man, H., Zhang, Q., and He, K.: Anthropogenic emission  
706 inventories in China: a review, *National Science Review*, 4, 834-866, 10.1093/nsr/nwx150, 2017a.

707 Li, M., Zhang, Q., Kurokawa, J. I., Woo, J. H., He, K., Lu, Z., Ohara, T., Song, Y., Streets, D. G., Carmichael, G. R., Cheng, Y., Hong, C.,  
708 Huo, H., Jiang, X., Kang, S., Liu, F., Su, H., and Zheng, B.: MIX: a mosaic Asian anthropogenic emission inventory under the international  
709 collaboration framework of the MICS-Asia and HTAP, *Atmos. Chem. Phys.*, 17, 935-963, 10.5194/acp-17-935-2017, 2017b.

710 Li, M., Zhang, Q., Streets, D. G., He, K. B., Cheng, Y. F., Emmons, L. K., Huo, H., Kang, S. C., Lu, Z., Shao, M., Su, H., Yu, X., and Zhang,  
711 Y.: Mapping Asian anthropogenic emissions of non-methane volatile organic compounds to multiple chemical mechanisms, *Atmos. Chem.*  
712 *Phys.*, 14, 5617-5638, 10.5194/acp-14-5617-2014, 2014.

713 Li, S., Wang, S., Wu, Q., Zhang, Y., Ouyang, D., Zheng, H., Han, L., Qiu, X., Wen, Y., Liu, M., Jiang, Y., Yin, D., Liu, K., Zhao, B., Zhang,  
714 S., Wu, Y., and Hao, J.: Emission trends of air pollutants and CO<sub>2</sub> in China from 2005 to 2021, *Earth Syst. Sci. Data*, 15, 2279-2294,  
715 10.5194/essd-15-2279-2023, 2023b.

716 Liu, F., Beirle, S., Zhang, Q., Dörner, S., He, K., and Wagner, T.: NO<sub>x</sub> lifetimes and emissions of cities and power plants in polluted  
717 background estimated by satellite observations, *Atmos. Chem. Phys.*, 16, 5283-5298, 10.5194/acp-16-5283-2016, 2016a.

718 Liu, F., Zhang, Q., Tong, D., Zheng, B., Li, M., Huo, H., and He, K. B.: High-resolution inventory of technologies, activities, and emissions  
719 of coal-fired power plants in China from 1990 to 2010, *Atmos. Chem. Phys.*, 15, 13299-13317, 10.5194/acp-15-13299-2015, 2015a.

720 Liu, H., Fu, M., Jin, X., Shang, Y., Shindell, D., Faluvegi, G., Shindell, C., and He, K.: Health and climate impacts of ocean-going vessels  
721 in East Asia, *Nature Climate Change*, 6, 1037-1041, 10.1038/nclimate3083, 2016b.

722 Liu, H., Meng, Z.-H., Lv, Z.-F., Wang, X.-T., Deng, F.-Y., Liu, Y., Zhang, Y.-N., Shi, M.-S., Zhang, Q., and He, K.-B.: Emissions and  
723 health impacts from global shipping embodied in US–China bilateral trade, *Nature Sustainability*, 2, 1027-1033, 10.1038/s41893-019-0414-  
724 z, 2019.

725 Liu, H., Wu, B., Liu, S., Shao, P., Liu, X., Zhu, C., Wang, Y., Wu, Y., Xue, Y., Gao, J., Hao, Y., and Tian, H.: A regional high-resolution  
726 emission inventory of primary air pollutants in 2012 for Beijing and the surrounding five provinces of North China, *Atmospheric*  
727 *Environment*, 181, 20-33, <https://doi.org/10.1016/j.atmosenv.2018.03.013>, 2018.

728 Liu, J., Zheng, Y., Geng, G., Hong, C., Li, M., Li, X., Liu, F., Tong, D., Wu, R., Zheng, B., He, K., and Zhang, Q.: Decadal changes in  
729 anthropogenic source contribution of PM<sub>2.5</sub> pollution and related health impacts in China, 1990–2015, *Atmos. Chem. Phys.*, 20, 7783-7799,  
730 10.5194/acp-20-7783-2020, 2020.

731 Liu, M., Song, Y., Yao, H., Kang, Y., Li, M., Huang, X., and Hu, M.: Estimating emissions from agricultural fires in the North China Plain  
732 based on MODIS fire radiative power, *Atmospheric Environment*, 112, 326-334, <https://doi.org/10.1016/j.atmosenv.2015.04.058>, 2015b.

733 Lu, Z., Zhang, Q., and Streets, D. G.: Sulfur dioxide and primary carbonaceous aerosol emissions in China and India, 1996–2010, *Atmos.*  
734 *Chem. Phys.*, 11, 9839-9864, 10.5194/acp-11-9839-2011, 2011.

735 Lv, Z., Liu, H., Ying, Q., Fu, M., Meng, Z., Wang, Y., Wei, W., Gong, H., and He, K.: Impacts of shipping emissions on PM<sub>2.5</sub> pollution  
736 in China, *Atmos. Chem. Phys.*, 18, 15811-15824, 10.5194/acp-18-15811-2018, 2018.

737 Mlawer, E. J., Taubman, S. J., Brown, P. D., Iacono, M. J., and Clough, S. A.: Radiative transfer for inhomogeneous atmospheres: RRTM,  
738 a validated correlated-k model for the longwave, *Journal of Geophysical Research: Atmospheres*, 102, 16663-16682,  
739 <https://doi.org/10.1029/97JD00237>, 1997.

740 Ni, H., Han, Y., Cao, J., Chen, L. W. A., Tian, J., Wang, X., Chow, J. C., Watson, J. G., Wang, Q., Wang, P., Li, H., and Huang, R.-J.:  
741 Emission characteristics of carbonaceous particles and trace gases from open burning of crop residues in China, *Atmospheric Environment*,  
742 123, 399-406, <https://doi.org/10.1016/j.atmosenv.2015.05.007>, 2015.

743 Ohara, T., Akimoto, H., Kurokawa, J., Horii, N., Yamaji, K., Yan, X., and Hayasaka, T.: An Asian emission inventory of anthropogenic  
744 emission sources for the period 1980–2020, *Atmos. Chem. Phys.*, 7, 4419-4444, 10.5194/acp-7-4419-2007, 2007.

745 Paulot, F., Jacob, D. J., Pinder, R. W., Bash, J. O., Travis, K., and Henze, D. K.: Ammonia emissions in the United States, European Union,  
746 and China derived by high-resolution inversion of ammonium wet deposition data: Interpretation with a new agricultural emissions inventory  
747 (MASAGE\_NH<sub>3</sub>), *Journal of Geophysical Research: Atmospheres*, 119, 4343-4364, <https://doi.org/10.1002/2013JD021130>, 2014.

748 Peng, L., Zhang, Q., Yao, Z., Mauzerall, D. L., Kang, S., Du, Z., Zheng, Y., Xue, T., and He, K.: Underreported coal in statistics: A survey-  
749 based solid fuel consumption and emission inventory for the rural residential sector in China, *Applied Energy*, 235, 1169-1182,  
750 <https://doi.org/10.1016/j.apenergy.2018.11.043>, 2019.

751 Pleim, J. E.: A Combined Local and Nonlocal Closure Model for the Atmospheric Boundary Layer. Part I: Model Description and Testing,  
752 *Journal of Applied Meteorology and Climatology*, 46, 1383-1395, 10.1175/JAM2539.1, 2007.

753 Reisen, F., Meyer, C. P., and Keyword, M. D.: Impact of biomass burning sources on seasonal aerosol air quality, *Atmospheric Environment*,  
754 67, 437-447, <https://doi.org/10.1016/j.atmosenv.2012.11.004>, 2013.

755 Schneider, A., Friedl, M. A., and Potere, D.: A new map of global urban extent from MODIS satellite data, *Environmental Research Letters*,  
756 4, 044003, 10.1088/1748-9326/4/4/044003, 2009.

757 Sha, Q., Zhu, M., Huang, H., Wang, Y., Huang, Z., Zhang, X., Tang, M., Lu, M., Chen, C., Shi, B., Chen, Z., Wu, L., Zhong, Z., Li, C., Xu,  
758 Y., Yu, F., Jia, G., Liao, S., Cui, X., Liu, J., and Zheng, J.: A newly integrated dataset of volatile organic compounds (VOCs) source profiles  
759 and implications for the future development of VOCs profiles in China, *Sci Total Environ*, 793, 148348, [10.1016/j.scitotenv.2021.148348](https://doi.org/10.1016/j.scitotenv.2021.148348),  
760 2021.

761 Song, Y., Liu, B., Miao, W., Chang, D., and Zhang, Y.: Spatiotemporal variation in nonagricultural open fire emissions in China from 2000  
762 to 2007, *Global Biogeochemical Cycles*, 23, GB2008, <https://doi.org/10.1029/2008GB003344>, 2009.

763 Streets, D. G., Bond, T. C., Carmichael, G. R., Fernandes, S. D., Fu, Q., He, D., Klimont, Z., Nelson, S. M., Tsai, N. Y., Wang, M. Q., Woo,  
764 J. H., and Yarber, K. F.: An inventory of gaseous and primary aerosol emissions in Asia in the year 2000, *Journal of Geophysical Research: Atmospheres*, 108, <https://doi.org/10.1029/2002JD003093>, 2003.

765 Tang, L., Jia, M., Yang, J., Li, L., Bo, X., and Mi, Z.: Chinese industrial air pollution emissions based on the continuous emission monitoring  
766 systems network, *Scientific Data*, 10, 153, [10.1038/s41597-023-02054-w](https://doi.org/10.1038/s41597-023-02054-w), 2023.

767 Trade, U. N. C. o. and Development: Review of Maritime Transport 2014, United Nations, <https://doi.org/10.18356/5a566ab1-en>, 2014.

768 Wang, W., Khanna, N., Lin, J., and Liu, X.: Black carbon emissions and reduction potential in China: 2015–2050, *Journal of environmental  
769 management*, 329, 117087, [10.1016/j.jenvman.2022.117087](https://doi.org/10.1016/j.jenvman.2022.117087), 2023.

770 Wang, X., Lei, Y., Yan, L., Liu, T., Zhang, Q., and He, K.: A unit-based emission inventory of SO<sub>2</sub>, NO<sub>x</sub> and PM for the Chinese iron and  
771 steel industry from 2010 to 2015, *Science of The Total Environment*, 676, 18–30, <https://doi.org/10.1016/j.scitotenv.2019.04.241>, 2019.

772 Wu, N., Geng, G., Qin, X., Tong, D., Zheng, Y., Lei, Y., and Zhang, Q.: Daily Emission Patterns of Coal-Fired Power Plants in China Based  
773 on Multisource Data Fusion, *ACS Environmental Au*, 2, 363–372, [10.1021/acsenvironau.2c00014](https://doi.org/10.1021/acsenvironau.2c00014), 2022.

774 Wu, N., Geng, G., Xu, R., Liu, S., Liu, X., Shi, Q., Zhou, Y., Zhao, Y., Liu, H., Song, Y., Zheng, J., and Zhang, Q.: INTAC: a high-resolution  
775 INTEgrated emission inventory of Air pollutants for China in 2017 [Data set], Zenodo, <https://doi.org/10.5281/zenodo.10459198>, 2024.

776 Wu, N., Geng, G., Yan, L., Bi, J., Li, Y., Tong, D., Zheng, B., and Zhang, Q.: Improved spatial representation of a highly resolved emission  
777 inventory in China: evidence from TROPOMI measurements, *Environmental Research Letters*, 16, 084056, [10.1088/1748-9326/ac175f](https://doi.org/10.1088/1748-9326/ac175f),  
778 2021.

779 Wu, Q., Han, L., Li, S., Wang, S., Cong, Y., Liu, K., Lei, Y., Zheng, H., Li, G., Cai, B., and Hao, J.: Facility-Level Emissions and Synergistic  
780 Control of Energy-Related Air Pollutants and Carbon Dioxide in China, *Environmental Science & Technology*, 57, 4504–4512,  
781 [10.1021/acs.est.2c07704](https://doi.org/10.1021/acs.est.2c07704), 2023.

782 Xiao, Q., Geng, G., Xue, T., Liu, S., Cai, C., He, K., and Zhang, Q.: Tracking PM<sub>2.5</sub> and O<sub>3</sub> Pollution and the Related Health Burden in  
783 China 2013–2020, *Environmental Science & Technology*, 56, 6922–6932, [10.1021/acs.est.1c04548](https://doi.org/10.1021/acs.est.1c04548), 2022.

784 Xiu, A. and Pleim, J. E.: Development of a Land Surface Model. Part I: Application in a Mesoscale Meteorological Model, *Journal of  
785 Applied Meteorology*, 40, 192–209, [10.1175/1520-0450\(2001\)040<0192:DOALSM>2.0.CO;2](https://doi.org/10.1175/1520-0450(2001)040<0192:DOALSM>2.0.CO;2), 2001.

786 Yang, Y. and Zhao, Y.: Quantification and evaluation of atmospheric pollutant emissions from open biomass burning with multiple methods:  
787 a case study for the Yangtze River Delta region, China, *Atmos. Chem. Phys.*, 19, 327–348, [10.5194/acp-19-327-2019](https://doi.org/10.5194/acp-19-327-2019), 2019.

788 Yin, L., Du, P., Zhang, M., Liu, M., Xu, T., and Song, Y.: Estimation of emissions from biomass burning in China (2003–2017) based on  
789 MODIS fire radiative energy data, *Biogeosciences*, 16, 1629–1640, [10.5194/bg-16-1629-2019](https://doi.org/10.5194/bg-16-1629-2019), 2019.

790 Zhang, J., Liu, L., Zhao, Y., Li, H., Lian, Y., Zhang, Z., Huang, C., and Du, X.: Development of a high-resolution emission inventory of  
791 agricultural machinery with a novel methodology: A case study for Yangtze River Delta region, *Environmental Pollution*, 266, 115075,  
792 <https://doi.org/10.1016/j.envpol.2020.115075>, 2020.

793 Zhang, Q. and Geng, G.: Impact of clean air action on PM<sub>2.5</sub> pollution in China, *Science China Earth Sciences*, 62, 1845–1846,  
794 [10.1007/s11430-019-9531-4](https://doi.org/10.1007/s11430-019-9531-4), 2019.

795 Zhang, Q., Streets, D. G., Carmichael, G. R., He, K. B., Huo, H., Kannari, A., Klimont, Z., Park, I. S., Reddy, S., Fu, J. S., Chen, D., Duan,  
796 L., Lei, Y., Wang, L. T., and Yao, Z. L.: Asian emissions in 2006 for the NASA INTEX-B mission, *Atmos. Chem. Phys.*, 9, 5131–5153,  
797 [10.5194/acp-9-5131-2009](https://doi.org/10.5194/acp-9-5131-2009), 2009.

798 Zhang, Q., Zheng, Y., Tong, D., Shao, M., Wang, S., Zhang, Y., Xu, X., Wang, J., He, H., Liu, W., Ding, Y., Lei, Y., Li, J., Wang, Z., Zhang,  
799 X., Wang, Y., Cheng, J., Liu, Y., Shi, Q., Yan, L., Geng, G., Hong, C., Li, M., Liu, F., Zheng, B., Cao, J., Ding, A., Gao, J., Fu, Q., Huo, J.,  
800 Liu, B., Liu, Z., Yang, F., He, K., and Hao, J.: Drivers of improved PM<sub>2.5</sub> air quality in China from 2013 to 2017, *Proc Natl Acad Sci U S  
801 A*, 116, 24463–24469, [10.1073/pnas.1907956116](https://doi.org/10.1073/pnas.1907956116), 2019a.

802 Zhang, Y., Bo, X., Zhao, Y., and Nielsen, C. P.: Benefits of current and future policies on emissions of China's coal-fired power sector  
803 indicated by continuous emission monitoring, *Environmental Pollution*, 251, 415–424, <https://doi.org/10.1016/j.envpol.2019.05.021>, 2019b.

804 Zhang, Y., Zhao, Y., Gao, M., Bo, X., and Nielsen, C. P.: Air quality and health benefits from ultra-low emission control policy indicated  
805 by continuous emission monitoring: a case study in the Yangtze River Delta region, China, *Atmos. Chem. Phys.*, 21, 6411–6430,  
806 [10.5194/acp-21-6411-2021](https://doi.org/10.5194/acp-21-6411-2021), 2021.

807 Zhao, Y., Mao, P., Zhou, Y., Yang, Y., Zhang, J., Wang, S., Dong, Y., Xie, F., Yu, Y., and Li, W.: Improved provincial emission inventory  
808 and speciation profiles of anthropogenic non-methane volatile organic compounds: a case study for Jiangsu, China, *Atmos. Chem. Phys.*,  
809 17, 7733–7756, [10.5194/acp-17-7733-2017](https://doi.org/10.5194/acp-17-7733-2017), 2017a.

810 Zhao, Y., Nielsen, C. P., Lei, Y., McElroy, M. B., and Hao, J.: Quantifying the uncertainties of a bottom-up emission inventory of  
811 anthropogenic atmospheric pollutants in China, *Atmos. Chem. Phys.*, 11, 2295–2308, [10.5194/acp-11-2295-2011](https://doi.org/10.5194/acp-11-2295-2011), 2011.

813 Zhao, Y., Qiu, L. P., Xu, R. Y., Xie, F. J., Zhang, Q., Yu, Y. Y., Nielsen, C. P., Qin, H. X., Wang, H. K., Wu, X. C., Li, W. Q., and Zhang,  
814 J.: Advantages of a city-scale emission inventory for urban air quality research and policy: the case of Nanjing, a typical industrial city in  
815 the Yangtze River Delta, China, *Atmos. Chem. Phys.*, 15, 12623-12644, 10.5194/acp-15-12623-2015, 2015.  
816 Zhao, Y., Xia, Y., and Zhou, Y.: Assessment of a high-resolution NOX emission inventory using satellite observations: A case study of  
817 southern Jiangsu, China, *Atmospheric Environment*, 190, 135-145, <https://doi.org/10.1016/j.atmosenv.2018.07.029>, 2018.  
818 Zhao, Y., Yuan, M., Huang, X., Chen, F., and Zhang, J.: Quantification and evaluation of atmospheric ammonia emissions with different  
819 methods: a case study for the Yangtze River Delta region, China, *Atmos. Chem. Phys.*, 20, 4275-4294, 10.5194/acp-20-4275-2020, 2020.  
820 Zhao, Y., Zhou, Y., Qiu, L., and Zhang, J.: Quantifying the uncertainties of China's emission inventory for industrial sources: From national  
821 to provincial and city scales, *Atmospheric Environment*, 165, 207-221, <https://doi.org/10.1016/j.atmosenv.2017.06.045>, 2017b.  
822 Zheng, B., Cheng, J., Geng, G., Wang, X., Li, M., Shi, Q., Qi, J., Lei, Y., Zhang, Q., and He, K.: Mapping anthropogenic emissions in China  
823 at 1 km spatial resolution and its application in air quality modeling, *Science Bulletin*, 66, 612-620, 10.1016/j.scib.2020.12.008, 2021.  
824 Zheng, B., Huo, H., Zhang, Q., Yao, Z. L., Wang, X. T., Yang, X. F., Liu, H., and He, K. B.: High-resolution mapping of vehicle emissions  
825 in China in 2008, *Atmospheric Chemistry and Physics*, 14, 9787-9805, 10.5194/acp-14-9787-2014, 2014.  
826 Zheng, B., Tong, D., Li, M., Liu, F., Hong, C., Geng, G., Li, H., Li, X., Peng, L., Qi, J., Yan, L., Zhang, Y., Zhao, H., Zheng, Y., He, K.,  
827 and Zhang, Q.: Trends in China's anthropogenic emissions since 2010 as the consequence of clean air actions, *Atmos. Chem. Phys.*, 18,  
828 14095-14111, 10.5194/acp-18-14095-2018, 2018.  
829 Zheng, B., Zhang, Q., Tong, D., Chen, C., Hong, C., Li, M., Geng, G., Lei, Y., Huo, H., and He, K.: Resolution dependence of uncertainties  
830 in gridded emission inventories: a case study in Hebei, China, *Atmos. Chem. Phys.*, 17, 921-933, 10.5194/acp-17-921-2017, 2017.  
831 Zheng, H., Cai, S., Wang, S., Zhao, B., and Hao, J.: Development of a unit-based industrial emission inventory in the Beijing–Tianjin–Hebei  
832 region and resulting improvement in air quality modeling, *Atmospheric Chemistry and Physics*, 19, 3447-3462, 2019.  
833 Zheng, J., He, M., Shen, X., Yin, S., and Yuan, Z.: High resolution of black carbon and organic carbon emissions in the Pearl River Delta  
834 region, China, *Science of The Total Environment*, 438, 189-200, <https://doi.org/10.1016/j.scitotenv.2012.08.068>, 2012.  
835 Zhou, Y., Xing, X., Lang, J., Chen, D., Cheng, S., Wei, L., Wei, X., and Liu, C.: A comprehensive biomass burning emission inventory with  
836 high spatial and temporal resolution in China, *Atmospheric Chemistry and Physics*, 17, 2839-2864, 2017a.  
837 Zhou, Y., Zhao, Y., Mao, P., Zhang, Q., Zhang, J., Qiu, L., and Yang, Y.: Development of a high-resolution emission inventory and its  
838 evaluation and application through air quality modeling for Jiangsu Province, China, *Atmos. Chem. Phys.*, 17, 211-233, 10.5194/acp-17-  
839 211-2017, 2017b.